The HERMES Polarized Hydrogen and Deuterium Internal Gas Target

HERMES Collaboration

A. Airapetian [r], N. Akopov [ad], Z. Akopov [ad], M. Amarian [h,ad], A. Andrus [p], E.C. Aschenauer [h], W. Augustyniak [ac], R. Avakian [ad], A. Avetissian [ad], E. Avetissian [ℓ], P. Bailey [p], D. Balin [u], C. Baumgarten [ae,aj], M. Beckmann [g], S. Belostotski [u], N. Bianchi [ℓ], H.P. Blok [t,ab], H. Böttcher [h], A. Borissov [o], A. Borysenko [ℓ], M. Bouwhuis [p], B. Braun [j], A. Brüll [q], V. Bryzgalov [v], G.P. Capitani [ℓ], M. Capiluppi [k], T. Chen [d], G. Ciullo [k], M. Contalbrigo [k], G. Court [af], P.F. Dalpiaz [k], R. De Leo [c], M. Demey [t], L. De Nardo [a], E. De Sanctis [ℓ], E. Devitsin [s], P. Di Nezza [ℓ], M. Düren [n], M. Ehrenfried [j], A. Elalaoui-Moulay [b], G. Elbakian [ad], F. Ellinghaus [h], U. Elschenbroich [m], R. Fabbri [t], A. Fantoni [ℓ], A. Fechtchenko [i], L. Felawka [z], S. Frullani [x], G. Gapienko [v], V. Gapienko [v], F. Garibaldi [x], K. Garrow [z], G. Gavrilov [g,z], V. Gharibyan [ad], G. Graw [ae], O. Grebeniouk [u], I.M. Gregor [h], C. Hadjidakis [ℓ], W. Haeberli [ag], K. Hafidi [b], M. Hartig [n], D. Hasch [ℓ], D. Heesbeen [t], M. Henoch [j], W.H.A. Hesselink [t,ab], A. Hillenbrand [j], M. Hoek [n], Y. Holler [g], B. Hommez [m], I. Hristova [h], G. Iarygin [i], A. Ivanilov [v], A. Izotov [u], H.E. Jackson [b], A. Jgoun [u], R. Kaiser [o], E. Kinney [f], A. Kisselev [f], T. Kobayashi [aa], N. Koch [j,ah], H. Kolster [ab,ae,ai], M. Kopytin [h], V. Korotkov [v], V. Kozlov [s], B. Krauss [j], V.G. Krivokhijine [i], L. Lagamba [c], L. Lapikás [t], A. Laziev [t,ab], P. Lenisa [k], P. Liebing [h], L.A. Linden-Levy [p], W. Lorenzon [r], H. Lu [e], J. Lu [z], S. Lu [n], B.-Q. Ma [d], B. Maiheu [m], N.C.R. Makins [p], Y. Mao [d], B. Marianski [ac], H. Marukyan [ad], V. Mexner [t], N. Meyners [g], R. Mussa [k], O. Mikloukho [u], C.A. Miller [a,z], Y. Miyachi [aa], V. Muccifora [ℓ], A. Nagaitsev [i], E. Nappi [c], Y. Naryshkin [u], A. Nass [j], M. Negodaev [h],

W.-D. Nowak [h], K. Oganessyan [g,ℓ], H. Ohsuga [aa], A. Osborne [o], N. Pickert [j], D.H. Potterveld [b], M. Raithel [j], D. Reggiani [k], P.E. Reimer [b], A. Reischl [t], A.R. Reolon [ℓ], C. Riedl [j], K. Rith [j], G. Rosner [o], A. Rostomyan [ad], L. Rubacek [n], J. Rubin [p], D. Ryckbosch [m], Y. Salomatin [v], I. Sanjiev [b,u], I. Savin [i], C. Schill [ℓ], G. Schnell [h], K.P. Schüler [g], J. Seele [p], R. Seidl [j], B. Seitz [n], R. Shanidze [j], C. Shearer [o], T.-A. Shibata [aa], V. Shutov [i], K. Sinram [g], W. Sommer [n], M. Stancari [k], M. Statera [k], E. Steffens [j], J.J.M. Steijger [t], H. Stenzel [n], J. Stewart [h], F. Stinzing [j], P. Tait [j], H. Tanaka [aa], S. Taroian [ad], B. Tchuiko [v], A. Terkulov [s], A. Trzcinski [ac], M. Tytgat [m], A. Vandenbroucke [m], P. van der Nat [t], G. van der Steenhoven [t], Y. van Haarlem [m], M.C. Vetterli [y,z], V. Vikhrov [u], M.G. Vincter [a], C. Vogel [j], J. Volmer [h], S. Wang [e], J. Wendland [y,z], J. Wilbert [j], T. Wise [ag], G. Ybeles Smit [ab], Y. Ye [e], Z. Ye [e], S. Yen [z], B. Zihlmann [m], P. Zupranski [ac]

[a] *Department of Physics, University of Alberta, Edmonton, Alberta T6G 2J1, Canada*

[b] *Physics Division, Argonne National Laboratory, Argonne, Illinois 60439-4843, USA*

[c] *Istituto Nazionale di Fisica Nucleare, Sezione di Bari, 70124 Bari, Italy*

[d] *School of Physics, Peking University, Beijing 100871, China*

[e] *Department of Modern Physics, University of Science and Technology of China, Hefei, Anhui 230026, China*

[f] *Nuclear Physics Laboratory, University of Colorado, Boulder, Colorado 80309-0446, USA*

[g] *DESY, Deutsches Elektronen-Synchrotron, 22603 Hamburg, Germany*

[h] *DESY Zeuthen, 15738 Zeuthen, Germany*

[i] *Joint Institute for Nuclear Research, 141980 Dubna, Russia*

[j] *Physikalisches Institut, Universität Erlangen-Nürnberg, 91058 Erlangen, Germany*

[k] *Istituto Nazionale di Fisica Nucleare, Sezione di Ferrara and Dipartimento di Fisica, Università di Ferrara, 44100 Ferrara, Italy*

[ℓ] *Istituto Nazionale di Fisica Nucleare, Laboratori Nazionali di Frascati, 00044 Frascati, Italy*

[m] *Department of Subatomic and Radiation Physics, University of Gent, 9000 Gent, Belgium*

[n] *Physikalisches Institut, Universität Gießen, 35392 Gießen, Germany*

[o] *Department of Physics and Astronomy, University of Glasgow, Glasgow G12 8QQ, United Kingdom*

[p] *Department of Physics, University of Illinois, Urbana, Illinois 61801-3080, USA*

[q] *Laboratory for Nuclear Science, Massachusetts Institute of Technology, Cambridge, Massachusetts 02139, USA*

[r] *Randall Laboratory of Physics, University of Michigan, Ann Arbor, Michigan 48109-1120, USA*

[s] *Lebedev Physical Institute, 117924 Moscow, Russia*

[t] *Nationaal Instituut voor Kernfysica en Hoge-Energiefysica (NIKHEF), 1009 DB Amsterdam, The Netherlands*

[u] *Petersburg Nuclear Physics Institute, St. Petersburg, Gatchina, 188350 Russia*

[v] *Institute for High Energy Physics, Protvino, Moscow region, 142281 Russia*

[w] *Institut für Theoretische Physik, Universität Regensburg, 93040 Regensburg, Germany*

[x] *Istituto Nazionale di Fisica Nucleare, Sezione Roma 1, Gruppo Sanità and Physics Laboratory, Istituto Superiore di Sanità, 00161 Roma, Italy*

[y] *Department of Physics, Simon Fraser University, Burnaby, British Columbia V5A 1S6, Canada*

[z] *TRIUMF, Vancouver, British Columbia V6T 2A3, Canada*

[aa] *Department of Physics, Tokyo Institute of Technology, Tokyo 152, Japan*

[ab] *Department of Physics and Astronomy, Vrije Universiteit, 1081 HV Amsterdam, The Netherlands*

[ac] *Andrzej Soltan Institute for Nuclear Studies, 00-689 Warsaw, Poland*

[ad] *Yerevan Physics Institute, 375036 Yerevan, Armenia*

[ae] *Sektion Physik, Universität München, 85748 Garching, Germany*

[af] *Physics Department, University of Liverpool, Liverpool L69 7ZE, United Kingdom*

[ag] *Department of Physics, University of Wisconsin-Madison, Madison, Wisconsin 53706 USA*

[ah] *Current address: Thales Electron Devices GmbH, Söflinger Str. 100, 89077 Ulm, Germany*

[ai] *Current address: Laboratory for Nuclear Science, Massachusetts Institute of Technology, Cambridge, Massachusetts 02139, USA*

[aj] *Current address: ACCEL Instruments GmbH, Friedrich-Ebert-Str. 1, D-51429 Bergisch Gladbach, Germany*

Abstract

The HERMES hydrogen and deuterium polarized gas targets have been in use since 1996 with the polarized electron beam of HERA at DESY to study the spin structure of the nucleon. The target employs of a storage cell internal to the HERA electron ring in which polarized atoms from a Stern-Gerlach Atomic Beam Source are injected. A sample beam diffuses from the center of the storage cell in a side tube to determine the atomic fraction and the atomic polarization. The atoms have a nuclear polarization whose axis is defined by an external magnetic holding field. The holding field has been longitudinal during 1996-2000 and it was changed to transverse in 2001. In the present paper, the setup of the target is described, the method for analyzing the target polarization is outlined, and the performance of the target in the different running periods is presented.

1 Introduction

The HERMES experiment at HERA (DESY, Hamburg) was designed to study the quark-gluon spin structure of the nucleon by deeply-inelastic scattering (DIS) of longitudinal polarized electrons from an internal polarized gas target of hydrogen and deuterium atoms [1,2]. The electron beam stored in the HERA storage ring with 27.5 GeV in energy and currents up to 50 mA is polarized by the Sokolov-Ternov effect [3] with a time constant of about 30 minutes yielding, in a machine with one spin rotator before the 2001 upgrade, a typical polarization of 60 %. A longitudinal spin direction within the HERA east straight section, where the experiment is located, is obtained by a pair of spin rotators [4].

The HERMES experiment [5], proposed in 1990, is designed to run in parallel to the two collider experiments, ZEUS and H1, without causing a significant reduction of the electron beam lifetime which is of the order of 10 hours. This limits the target areal density to about 10^{15} H $-$ atoms/cm^2 and excludes the use of any solid target material. A target employing a cold storage cell fed by a a polarized atomic beam source has been proposed and implemented. Polarized gas targets for storage rings were reviewed recently by Steffens and Haeberli [6].

During the first year of operation, 1995, the target was operated with polarized ^{3}He gas produced by a different source based on optical pumping [7]. Since 1996, the present target apparatus for polarized hydrogen and deuterium is in operation. During the years 1996-97 longitudinally polarized hydrogen ($H_{||}$) was used, while longitudinally polarized deuterium has been employed in 1998-2000 ($D_{||}$), and from 2001 on transversely polarized hydrogen ($H_{\perp}$) is under

study.

Apart from a high areal density and extreme reliability over many years, the most challenging requirement on the internal target was to determine the effective target polarization seen by the beam. The target polarization can not be measured by making use of scattering processes involving the high-energy electron beam due to the small cross sections involved. Nuclear vector polarization P_z and, for deuterium also tensor polarization P_{zz} were to be measured, plus the electron polarization P_e for diagnostic purposes. The required accuracy was $\delta P = 0.03$ absolute error on the average polarization over long measuring periods, and 1 % statistical accuracy within a couple of minutes in order to monitor possible changes in time. This goal was achieved by employing a sampling technique in conjunction with detailed simulations and frequent calibration measurements.

In the present article, an overview of the HERMES polarized hydrogen and deuterium gas target is given with reference to the various papers describing different subsystems of the target. The atomic beam source (ABS) [8], the storage cell [9], the Target Gas Analyzer (TGA) [10] and the Breit-Rabi polarimeter (BRP) [11] are summarized in Section 2. Section 3 describes the analysis applied to the raw TGA and BRP signals and the several calibrations required to derive measured values for the degree of dissociation , α^{TGA}, and the atomic polarization, P^{BRP}, of the sample gas. Section 4 reviews the various physical processes inside the storage cell which directly influence the TGA and BRP analyses [12–15]. The results of the target analysis are reported in Sections 6 and 7. Before the conclusions in Section 9, mention of some measurement collected by the HERMES detector with the polarized target will be given in Section 8.

2 Survey of experimental apparatus

The HERMES polarized hydrogen and deuterium target, schematically shown in Fig. 1, consists of an atomic beam source (ABS), which injects a spin polarized beam of H or D atoms into a thin walled storage cell. A sample of gas diffuses from the middle of the cell into a Breit Rabi Polarimeter (BRP), which measures the atomic polarization, or into a Target Gas Analyzer (TGA), which measures the relative atomic and molecular content of the gas. A magnet surrounding the storage cell provides a holding field defining the polarization axis and preventing spin relaxation by effectively decoupling the magnetic moments of electrons and nucleons. The HERMES experiment was provided with longitudinally polarized hydrogen/deuterium nuclei till the end of 2000. During the HERA shutdown in 2001, the target was converted to transverse polarization.

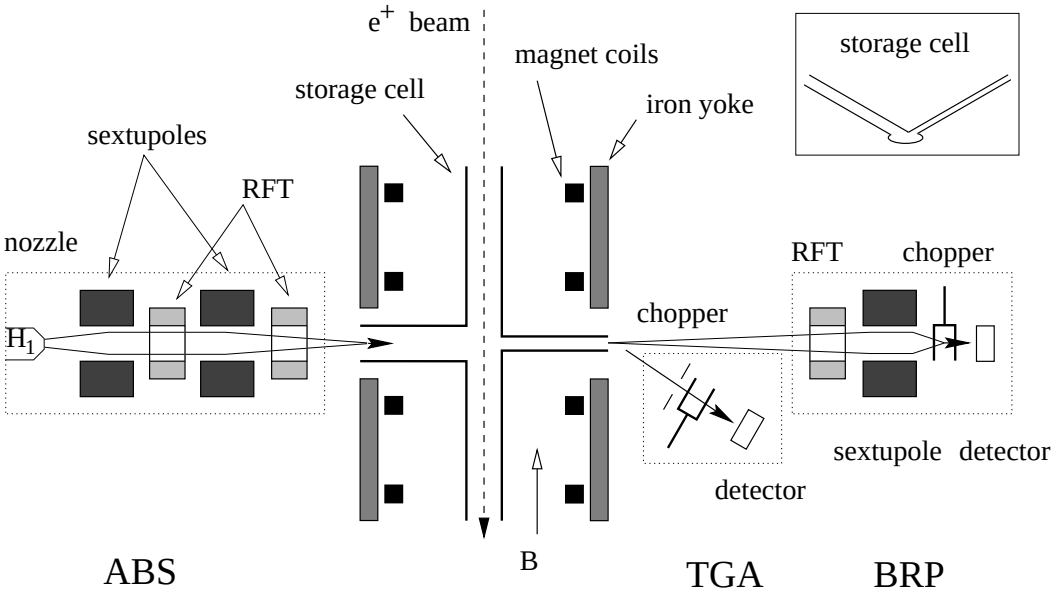

Fig. 1. Schematic view of the HERMES longitudinally polarized target. From left to right: Atomic Beam Source (ABS), target chamber with cell and magnet, diagnostic system composed by Target Gas Analyzer (TGA) and Breit-Rabi Polarimeter (BRP).

2.1 Target chamber

The target chamber, shown in Fig. 2 is evacuated by two turbo-molecular pumps with a combined speed of 4400 ls^{-1}. During operation the chamber pressure is typically in the 10^{-7} mbar range due to the high gas load from the atomic beam which enters the chamber under 30° above the horizontal plane. The storage cell and its supporting cooling rails are counter-levered from the upstream [1] end flange.

A thin walled exit window downstream of the target chamber allows the scattered electrons and hadronic fragments to leave the target chamber and to be detected by the HERMES spectrometer [5]. A fixed collimator (labeled as C2) protects the storage cell from direct synchrotron light of the HERA electron beam and from electrons hitting the cell wall. Further upstream of C2 an adjustable collimator (labeled as C1) with a more narrow opening is located which is opened up during electron injection into the HERA storage ring [5].

For longitudinal running the storage cell and vacuum chamber are immersed in a longitudinal field generated by a superconducting magnet. The magnet consists of four coils and an iron yoke designed to provide optimum field uniformity over the length of the storage cell while providing a central gap for

[1] upstream and downstream are used with respect to the HERA lepton beam direction

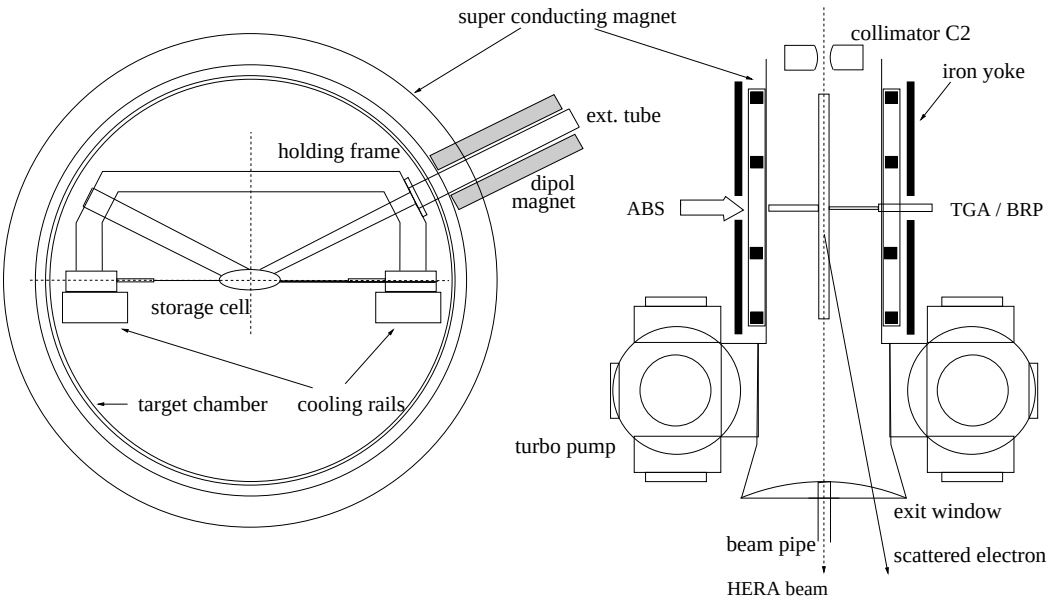

Fig. 2. Longitudinal target chamber and superconducting magnet viewed from downstream respect to the HERA beam direction (left) and from above (right).

the atomic beam to enter the cell. The magnetic field (up to 350 mT) provides the quantization axis for the spins of the polarized atoms in the storage cell and decoupling the spins of the nucleons and electrons. The passing HERA beam is bunched to provide high luminosity for the collider experiments H1 and ZEUS and, as it will discussed in Sec. 4.2.4, this may induce resonant nuclear depolarization of the target gas. The induced resonances can be avoided by proper setting of the holding field as long as its homogeneity is sufficient [13]. In case of hydrogen the maximum permissible variation of the magnetic field along the storage cell is 1.5%. For the running period with deuterium gas this requirement was found to be less critical [16].

2.2 Transverse magnet

After the end of the longitudinal running, the HERMES target was modified to enable the measurements with a hydrogen gas target in a transversally oriented magnetic holding field. The intensity of the transverse magnetic field was limited by the amount of synchrotron radiation power generated by the deflection of the beam by the target magnet (5 kW maximum), and it was decided to build a normal conducting magnet. As will be explained in Sec. 4.2.4, a higher homogeneity of the transverse target magnet of $\Delta B \leq 0.15$ mT at a field value of about 300 mT was required.

The geometrical constraints imposed by the larger HERMES acceptance made it more difficult to design a magnet fulfilling the uniformity requirement. After

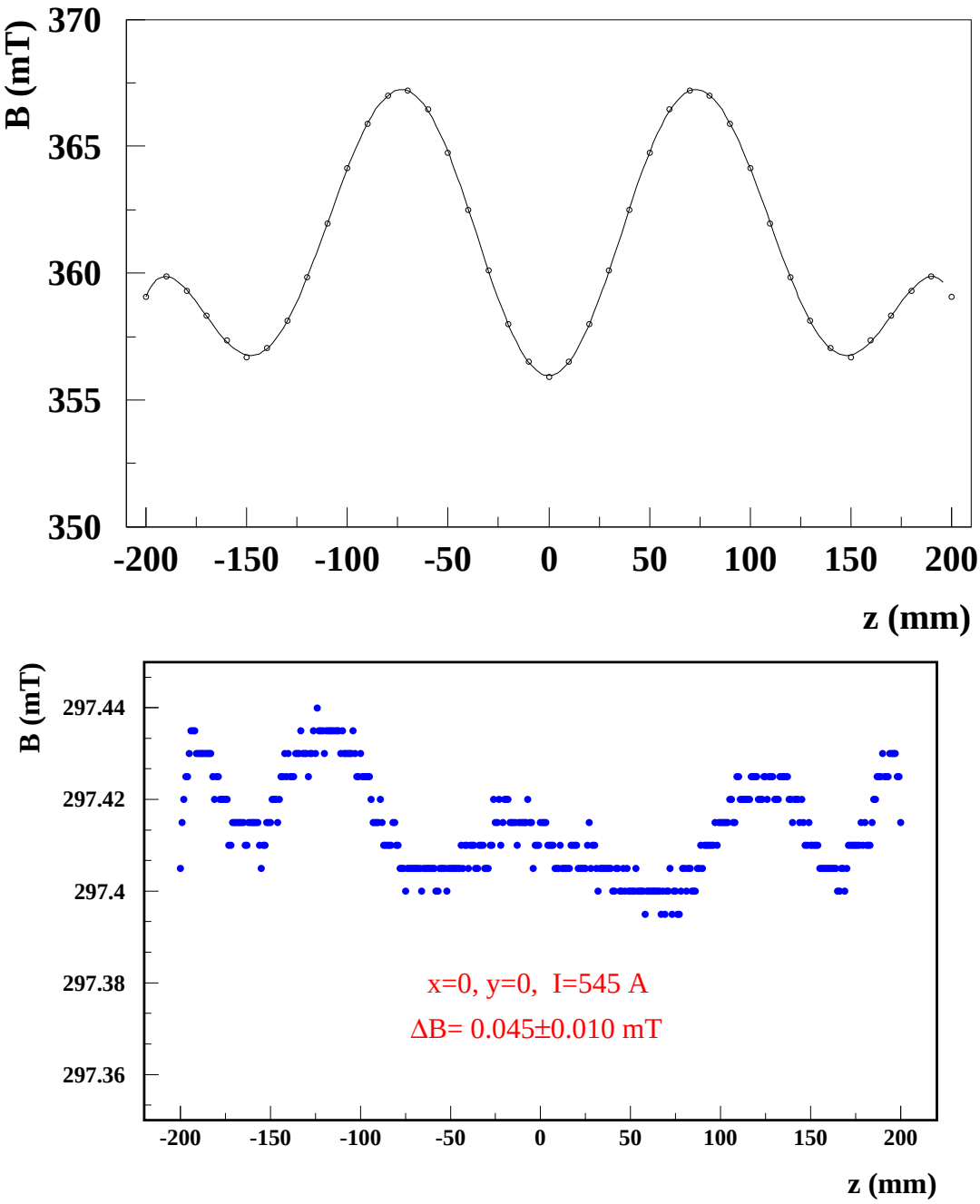

Fig. 3. Upper panel: field strength of the longitudinal target magnet measured along the HERA beam direction z covering the full length of the storage cell. The line shows a polynomial fit to the measurement. Lower panel: transverse magnet field uniformity measured along the z axis at the nominal field strength $B = 297\,\mathrm{mT}$. Deviations of $\Delta B_y = 0.15\,\mathrm{mT}$ (vert.) and $\Delta B_x = 0.60\,\mathrm{mT}$ (horiz.) have been measured within the cell volume.

period of use	cross section $a \times b$ (mm)	conductance (l/s)
05.96 - 11.99	29.8×9.8	$1.45\sqrt{T/M}$
01.99 (test)	19.8×8.0	$0.61\sqrt{T/M}$
12.99 - ...	21.0×8.9	$0.80\sqrt{T/M}$

Table 1
The history of cells used by HERMES. The lengths of the major and minor axes of the ellipse are indicated by a and b; T is the temperature of the cell in K, and M is the atomic mass of the gas in amu.

the construction, the field uniformity was measured and improved by shimming the pole tips. At a field strength of B=297 mT, deviations of ΔB_z=0.05 mT, ΔB_y=0.15 mT, ΔB_x=0.60 mT within the storage cell volume have been achieved, z being the longitudinal direction, y the transverse and x the horizontal axis. The magnet has been installed in the HERMES hydrogen target in July 2001. The strength of the transverse field vs. z is shown in the lower plot of Fig. 3.

2.3 The storage cell

The HERMES storage cell [9] is made of two 75 μm thin pure aluminum sheets which are tightly spot-welded together. It is 400 mm long and has an elliptical cross section shape of 21 × 8.9 mm^2. All the aluminum parts of the cell are coated with Drifilm [17] to minimize depolarization and recombination caused by wall collisions [18–21]. The cell wall extends partly about 147 mm downstream of the cell to ensure that all scattered particles inside the spectrometer detector acceptance pass through the same thickness of material (see Fig. 4).

Cells with three different elliptical cross sections have been used so far. The mentioned size of 21 × 8.9 mm^2 is the one which is in use since December 1999, called the medium-sized cell. The "large-size" which was used until December 1999 had a cross section of 29 × 9.8 mm^2 and a "small-one" (19 × 8.0 mm^2) was tested in January 1999 and found to be too small. Table 1 summarizes dimensions and conductances of the different cells which has been used. The conductance refers to gas injected into the cell center.

Wake field suppressors made of 100 μm thick titanium confine the electromagnetic high frequency field of the bunched HERA beam and form an electrical "smooth" connection between the storage cell and the HERA beam pipe.

The storage cell is mounted onto cooling rails which are cooled by temperature regulated gaseous helium. The optimum operating temperature for hydrogen targets was found to be about 100 K where recombination and depolarization

effects are low. Additionally, the lower conductance at this temperature leads to a higher target thickness by a factor $\sqrt{3}$ as compared to room temperature. For deuterium gas the target temperature could be decreased further to about 65 K which increased the target thickness by about 23 % compared to 100 K.

The temperature of the cooling rails is monitored at three different positions by platinum resistors. Since 1999 an additional thermocouple wire is attached to the aluminum foil close to the cell ellipse to monitor the cell temperature directly during the injection of the HERA beam when a temperature raise of about 5-10 K is usually detected. The cooling rails are connected to the target chamber flange on the upstream end. Due to thermal contraction of the cell when being cooled, the position of the cell center changes relative to the atomic beam source and the Breit-Rabi polarimeter. From room temperature down to 100 K the cell center moves by 0.9 mm. The alignment of atomic beam source and Breit-Rabi polarimeter relative to the cell center includes an offset to compensate for this effect at the target working point.

The cell is shown along with its support flange in Fig. 4. Two side tubes are connected to the beam tube, one to inject the polarized atoms through the injection tube and another, smaller one, to sample about 5% of the target gas and analyze it in the target gas analyzer and the Breit-Rabi polarimeter. The sample tube is tilted 120° with respect to the axis of the injection tube to ensure that the sampled atoms have thermalized with the storage cell wall. A permanent dipole magnet around the extension tube outside the target chamber extends the magnetic holding field of the target magnet to prevent depolarization inside the extension tube (see Fig. 2). A capillary near the location of the feed tube allows injection of unpolarized gas into the cell.

2.4 Atomic Beam Source

The atomic beam source [8] consists of dissociator, a powerful differential pumping system, a beam forming system; a sextupole magnet system to focus atoms with $m_S = +\frac{1}{2}$ into the storage cell and adiabatic high-frequency transitions to manipulate the hyperfine population of the atomic beam. With the HERMES setup, injected fluxes of $\Phi^{ABS} \approx 6.5 \times 10^{16}$ atoms/s in case of hydrogen (2 states) and $\Phi^{ABS} \approx 4.5 \times 10^{16}$ atoms/s in case of deuterium (3 states) have been observed. These values are calculated from the density-dependent spin exchange relaxation [16]. The injected nuclear polarization P_z^{inj} was constantly above 0.97 for hydrogen and above 0.91 for deuterium. A schematic picture of the ABS setup is depicted in Fig. 5.

Pure molecular hydrogen/deuterium gas enters the dissociator from the left. The molecules are dissociated by a radio frequency discharge with a frequency

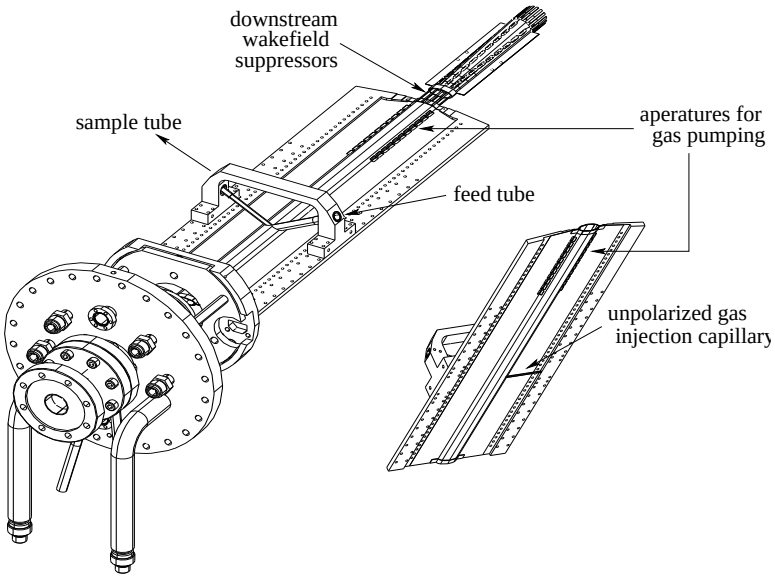

Fig. 4. The storage cell and its support flange.

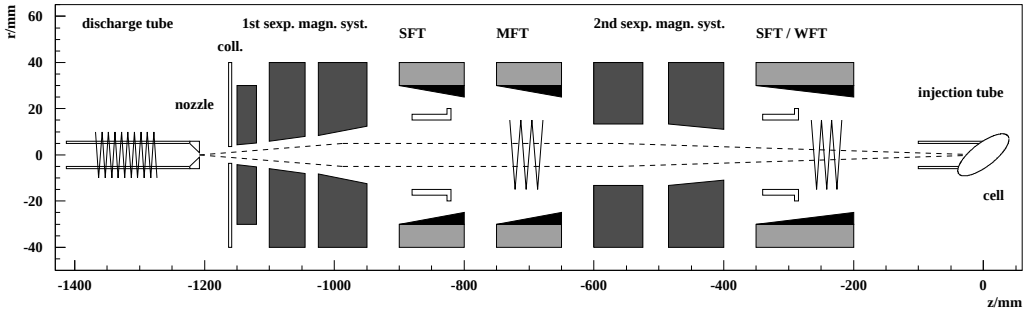

Fig. 5. Schematic view (from downstream of the electron beam) of the HERMES ABS with dissociator and collimator for beam formation. Two sets of sextupole magnets are located along the beam axis as are the high-frequency transitions. The axis of the ABS is tilted by 30° downwards with respect to the horizontal plane.

of 13.56 MHz in a pyrex tube of the dissociator with a degree of dissociation up to 80 % (H_2,D_2) at a throughput of about 1 mbar l s^{-1} and radio frequency powers of 300 W. To maximize the stability and the degree of dissociation an amount of oxygen between 0.1 and 0.3 volume percent is added to the molecular gas.

A high degree of dissociation at higher throughput can be achieved using a recently developed microwave (MW) dissociator [22]. The microwave dissociator operates at a frequency of 2.45 GHz. With typical throughputs between 1 mbar l s^{-1} and 2 mbar l s^{-1} and microwave powers of about 600 W a degree of dissociation higher than 80 % is achieved. The MW dissociator has been used in the 2000 running with deuterium while the RF dissociator has been

used for the rest of the data taking.

The atomic gas flows through a conical nozzle with an opening diameter of 2 mm which is cooled to about 100 K. The water produced in the discharge then freezes at the nozzle and reduces surface recombination. The ice layer continuously thickens and slowly reduces the gas conductance of the nozzle. After typically 3-5 days of operation the pressure in the dissociator tube rises substantially to increase volume recombination in the tube, resulting in a noticeable decrease in the degree of dissociation of gas exiting the nozzle. Full recovery is achieved by slightly warming up the nozzle to remove the ice layer.

After passing the cold nozzle the gas expands into the vacuum of the dissociator chamber. A powerful differential pumping system with a total nominal pumping speed of more than 15000 ls^{-1} ensures low gas flow into the HERA vacuum system.

The magnet system of the HERMES atomic beam source consists of a total of five Halbach [23] type segmented permanent sextupole magnets with a maximum poletip field of about 1.5 T. Every magnet consists of 24 segments of *Vacodym*[2] . Four high frequency transition units are available: two in between the sextupole magnets and two after the last magnet. The system provides enough flexibility that many different combination of hyperfine population can be injected into the cell. Between the sextupoles, a strong field transition (SFT) and a medium field transition (MFT) can be used simultaneously whereas the weak field transition (WFT) and the SFT after the sextupole magnets can only be used separately, because they share the coils for the static and gradient magnetic fields. The complete set of possible hyperfine populations that can be produced is shown in Tab. 2.

2.5 Target Gas Analyzer

The target gas analyzer (TGA) [10] measures the atomic and the molecular content of the gas extracted from the storage cell by the sample and extension tubes.

The TGA setup, shown in Fig. 7, consists of a pair of baffles, a chopper, a 90° off-axis quadrupole mass spectrometer (QMS) with a cross beam ionizer and a channel electron multiplier (CEM) for single ion detection.

The TGA is integrated into the vacuum system of the BRP sextupole chamber, which is served by two cryo pumps and a titanium sublimation pump, with a total pumping speed of about 7000 ls^{-1}. During operation, the pressure is in

[2] Vacodym is a registered trademark of Vacuumschmelze GmbH, Hanau, Germany

the TGA detector is about $4{\cdot}10^{-9}$ mbar. Prior to normal operation, the TGA vacuum chamber is backed out with temperatures up to 180 °C for 48 hours. The BRP/TGA vacuum scheme is shown in Fig. 8.

Gas	HFT (betw. 6-poles)	HFT (after 6-poles)	Inj. States	P_e	P_z	P_{zz}	Use
H	-	-	$\|1\rangle$, $\|2\rangle$	+1	0	-	Cal
	-	WFT 1-3	$\|2\rangle$, $\|3\rangle$	0	-1	-	Data
	-	SFT 2-4	$\|1\rangle$, $\|4\rangle$	0	+1	-	Data
	SFT 2-4 / MFT 2-3	-	$\|1\rangle$	+1	+1	-	Cal
	WFT 1-3 / MFT 1-3	-	$\|2\rangle$	+1	-1	-	Cal
	SFT 2-4 / MFT 2-3	WFT 1-3	$\|3\rangle$	-1	-1	-	Cal
	WFT 1-3 / MFT 1-3	SFT 2-4	$\|4\rangle$	-1	+1	-	Cal
	WFT 1-3, SFT 2-4	-	*no state*	-	-	-	Cal
D	-	-	$\|1\rangle$ $\|2\rangle$ $\|3\rangle$	+1	0	0	Cal
	SFT 2-5	WFT 1-4	$\|3\rangle$ $\|4\rangle$	0	-1	+1	Data
	SFT 3-5	SFT 2-6	$\|1\rangle$ $\|6\rangle$	0	+1	+1	Data
	MFT 1-4	SFT 3-5	$\|2\rangle$ $\|5\rangle$	0	0	-2	Data
	MFT 1-4	SFT 2-6	$\|3\rangle$ $\|6\rangle$	0	0	+1	Data
	MFT 3-4, SFT 2-6	-	$\|1\rangle$	+1	+1	+1	Cal
	WFT 1-4, SFT 2-6	-	$\|2\rangle$	+1	0	-2	Cal
	WFT 1-4, SFT 3-5	-	$\|3\rangle$	+1	-1	+1	Cal
	MFT 3-4, SFT 2-6	WFT 1-4	$\|4\rangle$	-1	-1	+1	Cal
	WFT 1-4, SFT 3-5	SFT 3-5	$\|5\rangle$	+1	0	-2	Cal
	WFT 1-4, SFT 2-6	SFT 2-6	$\|6\rangle$	-1	+1	+1	Cal

Table 2
Injection modes of the atomic beam source. The table shows the high frequency transition units employed (2^{nd} and 3^{rd} column), the hyperfine states injected in the target cell and the resulting electron (P_e), nuclear (P_z) and tensor (P_{zz}) polarizations in the ideal case of 100 % efficient sextupole system and transition units, no depolarization inside the target cell and infinitely strong guide field. The last column clarifies the purpose of each mode (Cal: calibration, monitoring; Data: HERMES data taking). The injection modes for hydrogen and deuterium single states are listed separately. For some modes the MFT between the sextupoles has to be tuned as a WFT 1-4. The *no state* injection mode is only possible for hydrogen and has been operational since April 2002. The adopted labeling for the hyperfine states is explained in the Breit-Rabi diagram of Fig. 6

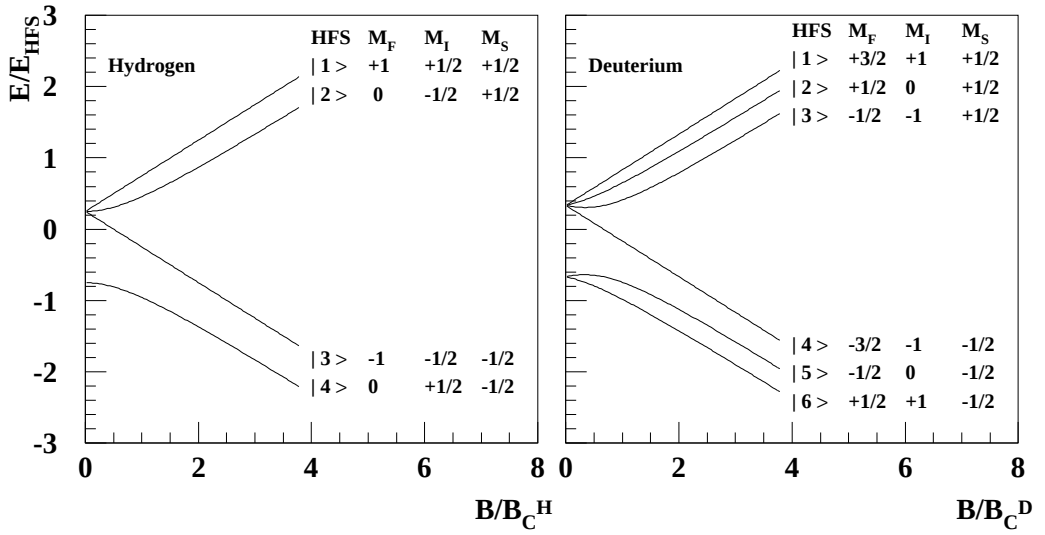

Fig. 6. Hyperfine energy levels of hydrogen (left) and deuterium (right) atoms as a function of the magnetic holding field (Breit-Rabi diagram) and corresponding labeling. The field values are scaled with the corresponding critical field and energy values with the corresponding hyperfine energy.

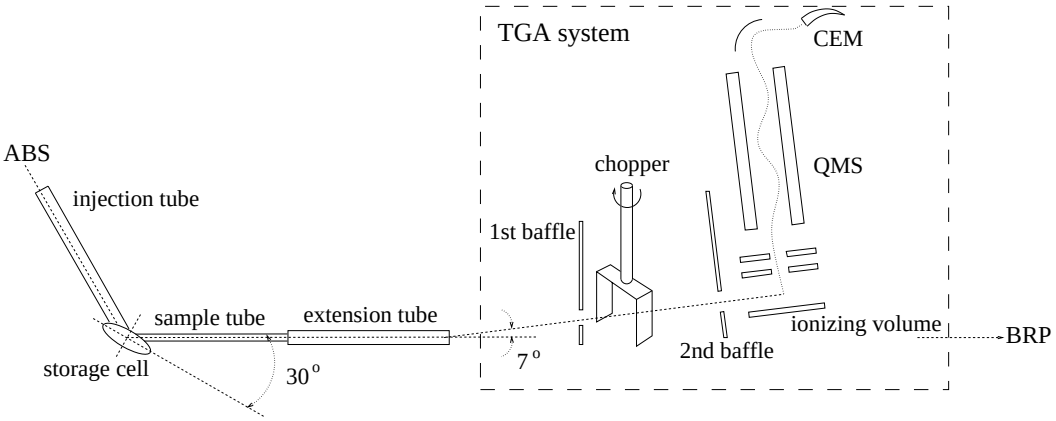

Fig. 7. A schematic diagram of the Target Gas Analyzer. The gas of atoms and molecules diffuses through the extension tube and is collimated by two baffles before entering the ionizing volume. The chopper is used for background subtraction

The TGA is mounted 7° off-axis with respect to the BRP, in order not to interfere with the beam entering the polarimeter. The first baffle ensures that only gas from the sample beam can reach the detector, while the second one acts as a collimator, so that no atoms can hit the metal parts of the ionizer and recombine. The chopper, placed between the two baffles, rotates at a frequency of 5.5 Hz, thus periodically blocking the sample beam in order to allow subtraction of the residual gas signal. Particles entering the detector are ionized by 70 eV electrons, mass filtered with the QMS, and finally detected by the CEM. The pulses are counted by a 2048 bin time resolving counter (TRC). The bin length is typically set to 175 μs so that two chopper turns are

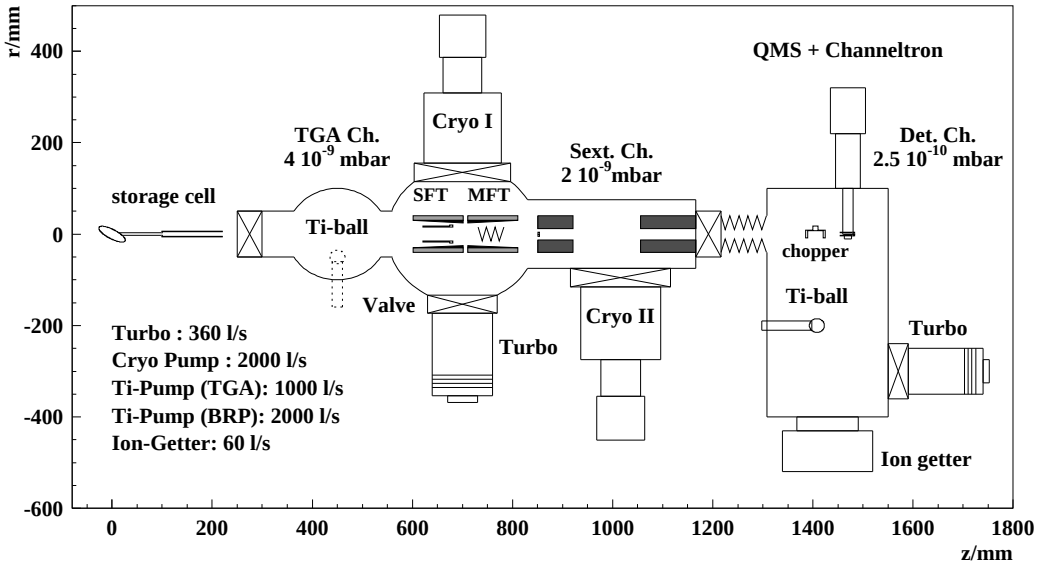

Fig. 8. Schematic view of the BRP/TGA vacuum system.

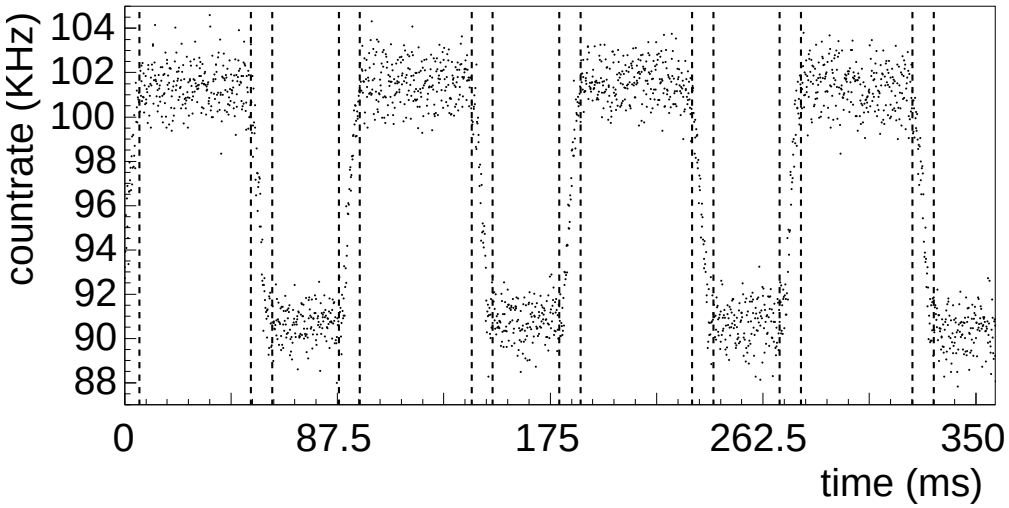

Fig. 9. Time spectrum of atomic count rates in the TGA. The vertical lines indicate the binning used to define the chopper positions open, undefined and closed.

collected within the whole bin range as shown in Fig. 9. The synchronization between chopper status and counting rate is given by a trigger signal coming from the chopper motor. The beam rate is calculated by taking the difference between the number of counts collected with the chopper open and closed.

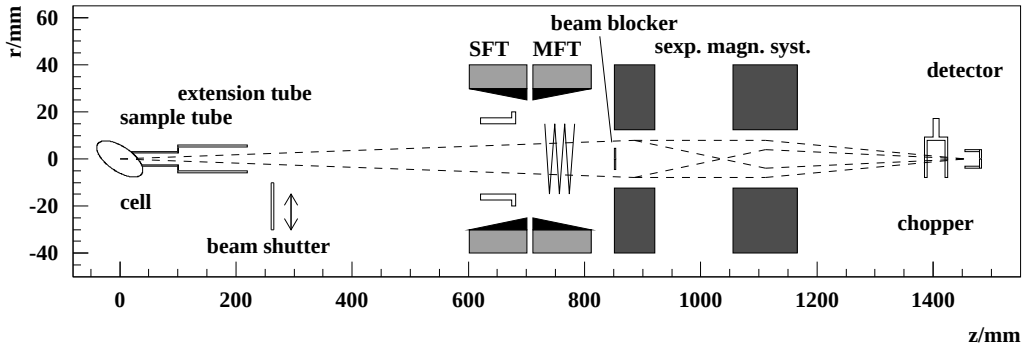

Fig. 10. Schematic layout of the BRP. The rf-transition units extend from z = 600 to 810 mm. The beam blocker at the entrance to the first 6-pole magnet ensures 100 % rejection of atoms with $m_s = -\frac{1}{2}$. The beam shutter is used to measure the hydrogen contribution coming from dissociative water ionization.

2.6 Breit-Rabi Polarimeter

The Breit-Rabi polarimeter (BRP) [11] measures the relative populations n_i of the hyperfine states of hydrogen (or deuterium) atoms contained in the sample beam. From this measurement, the absolute atomic polarization can be calculated by applying the knowledge of the target magnetic field strength.

A schematic view of the BRP is shown in Fig. 10. The sample beam, from left to right, leaves the extension tube of the target cell encountering first two hyperfine transition units, then a sextuple magnet system and eventually the detector stage.

A differential pumping system keeps - during operation - the pressure at $2{\times}10^{-9}$ mbar in the sextupole chamber and at $2.5{\times}10^{-10}$ mbar in the detector chamber.
Two transition units are used to exchange the populations between pairs of hyperfine states: a strong field transition unit (SFT) with tilted resonator which can be tuned for both π and σ transitions, and a medium field transition (MFT) unit which can induce different π transitions according to the static field strength and gradient setting used. The sextupole system, composed of two magnets, spin filters the sample beam by focusing atoms with $m_s = +\frac{1}{2}$ towards the BRP geometrical axis and defocusing atoms with $m_s = -\frac{1}{2}$ away. A 9 mm diameter beam blocker placed in front of the first sextupole magnet ensures that no atoms in $m_s = -\frac{1}{2}$ states can reach the detector. The sextupole system has been redesigned in the year 2000 in order to improve the transmission probability at the typical HERMES working temperature. The detector stage is identical to the one employed for the target gas analyzer: a cross beam ionizer, a quadrupole mass spectrometer (QMS) and a channel electron multiplier (CEM). In contrast to the TGA, only hydrogen (or deuterium) *atoms*

are detected by the BRP. The chamber residual gas correction is carried out by using a chopper in the same way as described for the TGA. An additional beam shutter, placed just after the extension tube exit, is used to measure the possible contribution of atomic hydrogen coming from the dissociation of H_2O and H_2 (D_2O, DHO, D_2 and DH in the deuterium case) present on the vacuum chambers walls [3].

3 Analysis of TGA and BRP signals

3.1 Interpretation of the TGA signals

The measured TGA atomic (molecular) signal S_a (S_m) is proportional to the product of the *particle* flux Φ_a (Φ_m) into the TGA, the mean inverse velocity of the particles $\langle\frac{1}{v_a}\rangle$ ($\langle\frac{1}{v_m}\rangle$), the ionization cross section σ_a^{ion} (σ_m^{ion}) and the detection probability ϵ_a (ϵ_m). The dependence of the signal on the emission current which also exists, is measured and taken into account by the normalization function $f(I_{emiss})$. Taking all parameters into account one finds:

$$S_{a,m} \propto f(I_{emiss})\ \sigma_{a,m}^{ion}\ \epsilon_{a,m}\ \left\langle \frac{1}{v_{a,m}} \right\rangle \Phi_{a,m}. \tag{1}$$

The total flux of H or D nucleons into the TGA, Φ^{TGA}, can be related to the fluxes of particles, Φ_a and Φ_m, by:

$$\Phi^{TGA} = \Phi_a + 2\Phi_m. \tag{2}$$

The TGA geometrical acceptance is such that detected particles have bounced, on average, more than 100 times onto the extension tube inner surface [16]. For this reason, particles entering the TGA detector have thermalized with the extension tube wall.

For thermalized atoms and molecules one has:

$$\left\langle \frac{1}{v_m} \right\rangle = \sqrt{2} \left\langle \frac{1}{v_a} \right\rangle. \tag{3}$$

[3] The beam shutter was installed at the beginning of the deuterium running period, in 1998. During the 1996/'97 hydrogen running period, the contribution of dissociative hydrogen ionization was taken into account by detecting the amount of masses 2 and 18 amu in addition to mass 1 amu [16].

Using Eqs. (1), (2) and (3), it can be shown that the partial beam rates S_a S_m can be combined to form the variable S_{tot} which is proportional to Φ^{TGA}:

$$S_{tot} = S_a + \kappa\sqrt{2}S_m \propto \Phi^{TGA}, \tag{4}$$

where κ is the calibration constant of the TGA giving the relative sensitivity of the TGA for atomic and molecular beams:

$$\kappa = \frac{\sigma_a^{ion}\ \epsilon_a}{\sigma_m^{ion}\ \epsilon_m}. \tag{5}$$

In Eq.5 the σ's are the cross-sections and the ϵ's are the combined collection and transmission efficiencies.

Eq. 4 applies to the case of constant extension tube temperature, T_{ext}, and emission current, I_{emiss}. Taking into account the dependence of S_a, S_m on the measured[4] T_{ext} and I_{emiss} one can define a temperature and emission normalized nucleon flow rate, ϕ_{tot}, proportional to the injected ABS intensity Φ_{ABS}:

$$\phi_{tot} = \frac{S_{tot}\sqrt{T_{ext}}}{f(I_{emiss})} \propto \Phi^{TGA} \tag{6}$$

ϕ_{tot} is a good monitor of ABS stability over time as it is independent of recombination inside the storage cell. Following Eq. 4 one can also express normalized nucleon flow rates as atoms, ϕ_a, and as molecules, ϕ_m, by:

$$\phi_a = \frac{S_a\sqrt{T_{ext}}}{f(I_{emiss})} \tag{7}$$

$$\phi_m = \frac{\sqrt{2}\kappa S_m\sqrt{T_{ext}}}{f(I_{emiss})}. \tag{8}$$

The degree of dissociation of the sample beam, defined as the fraction of nucleons in atoms relative to all nucleons entering the TGA, is given by

$$\alpha^{TGA} = \frac{\phi_a}{\phi_a + \phi_m} = \frac{S_a}{S_a + \sqrt{2}\,\kappa\ S_m}. \tag{9}$$

[4] A thermocouple on the extension tube was first installed at the beginning of 1999. In the 1997 analysis, the extension tube temperature has been derived using the expression $T_{ext}(T) = T_0 + \frac{300-T_0}{300}T$, where T_0 is a constant and T is the measured cell temperature in K

target/year	κ
$H_{\|\|}(1997)$	0.551 ± 0.026
$D_{\|\|}(2000)$	0.861 ± 0.024
$H_{\perp}(2002)$	0.55 ± 0.05

Table 3
Summary of the values of TGA calibration constant k for the years 1997-2002.

The degree of dissociation α^{TGA}, also called atomic fraction, is displayed by the TGA roughly once per minute.

3.2 The calibration of the TGA

The purpose of the TGA calibration is to determine the relative sensitivity κ defined by (5). The calibration can be performed by varying the relative amount of atoms and molecules at a constant injected ABS total flux:

$$\phi_{tot} = \phi_a + \phi_m = const. \tag{10}$$

Using the relations (7) and (8), one can write

$$\frac{\partial\left(\frac{S_m}{g(T_{ext})\ f(I_{emiss})}\right)}{\partial\left(\frac{S_a}{g(T_{ext})\ f(I_{emiss})}\right)} = -\frac{1}{\sqrt{2}\,\kappa}, \tag{11}$$

where the minus sign reflects the fact that an increase in the ϕ_m must correspond to a decrease of ϕ_a. Hence a fit over the normalized molecular signal, ϕ_m as function of the normalized atomic one, ϕ_a results in a straight line with a slope of $-\frac{1}{\sqrt{2}\,\kappa}$.
Because the recombination process in the HERMES target is strongly temperature dependent, a variation of the atomic fraction can be obtained in a controllable way by changing the temperature of the storage cell. A second possibility is to take advantage of an accidental beam loss in the region of the HERMES target which might temporarily change the surface property of the cell and cause a sharp drop of α^{TGA} followed by a slow recovery. This beam loss calibration method does not require any knowledge about the temperature correction function $g(T_{ext})$. The measured values for k are reported in Tab. 3.

A detailed description about the TGA performance and its calibration can be found in Ref. [10].

3.3 Interpretation of BRP signals

The atomic signal detected by the BRP depends on the hyperfine population in the sample beam, on the transmission probabilities of the sextupole system and on the setting of the transition units. For a stable storage cell temperature, the transmission of the magnetic system is fixed. On the contrary, the transition units can be switched on and off, changing the intensity of the beam reaching the detector. The BRP signal can be described by the following expression:

$$S_i = c \sum_a \left(\sum_b \sigma_b T^i_{ab} \right) I_a, \tag{12}$$

where I_a is the sample beam intensity (in atoms/s) of the atoms in hyperfine state $|\, a \,\rangle$, T^i_{ab} describes the exchange of hyperfine states by the transition unit [5] i, σ_b is the sextupole transmission probability for state $|\, b \,\rangle$, and c is a proportionality factor [6]. The goal of these measurements is to determine the four (six) sample beam intensities, I_a, for the hydrogen (deuterium) sample beam. Summing Eq. 12 over index b one obtains:

$$S_i = c \sum_a M_{ia} I_a, \tag{13}$$

where the *measurement matrix* M_{ia} includes information concerning transmission probabilities and RF-transition efficiencies.
Assuming that M_{ia} is known, one can solve the system of equations (13) for I_a if, during a given ABS injection status, the BRP transition units are operated in at least four (six) different modes in case of hydrogen (deuterium).
The solution is given by

$$I_a = c^{-1} \sum_i R_{ai} S_i, \tag{14}$$

where [7] $R = M^{-1}$. The total sample beam intensity, I_{tot}, is obtained by the taking the sum over all hyperfine states:

$$I_{tot} = \sum_a I_a. \tag{15}$$

[5] If both units are working, the matrix T^i has to be replaced by $A = \prod_i T^{(i)}$

[6] The expression (12) simplifies into $S_{off} = c \sum_a \sigma_a I_a$ in case that no transition unit is switched on.

[7] If the number of collected signals is larger than the number of unknowns, one has to use the *pseudo-inverse* matrix $R = (M^T G_S M)^{-1} M^T G_S$, where G_S is the inverse covariance matrix of the measured signals. This procedure is equivalent to a fit of the intensities I_a to the signals S_i.

Finally, the relative hyperfine populations n_a are given by normalizing the intensities I_a:

$$n_a = \frac{I_a}{I_{tot}}. \tag{16}$$

The polarization of the atoms in the sample beam can now be calculated from the target magnetic field strength, as expressed by the following vectorial forms for hydrogen and deuterium, respectively:

$$(P_e, P_z)^T = M_P^H (n_1, n_2, n_3, n_4)^T \tag{17}$$
$$(P_e, P_z, P_{zz})^T = M_P^D (n_1, n_2, n_3, n_4, n_5, n_6)^T, \tag{18}$$

where the matrices M_P^H and M_P^D contain the target holding field strength. e.g. for hydrogen:

$$\mathbf{M_P^H} = \begin{pmatrix} -1 & a & 1 & -a \\ 1 & -a & -1 & a \end{pmatrix}, \tag{19}$$

where a $= \frac{\chi}{\sqrt{1+\chi^2}}$, $\chi = B/B_c$, $B_c = 50.7$ mT.

The statistical errors of the measured signals S_i are represented by the diagonal covariance matrix C_S. Hence, the covariance error matrix C_I of the intensities I_a is given by:

$$C_I = R C_S R^T = (M^T C_S^{-1} M)^{-1}. \tag{20}$$

The sum over all the elements of C_I gives the statistical error ΔI_{tot} of the total intensity I_{tot}:

$$\Delta I_{tot} = \sum_{ab} (C_I)_{ab}. \tag{21}$$

The covariance matrix C_N of the hyperfine populations n_a is

$$(C_N)_{ab} = \sum_{cd} \left(\frac{\partial n_a}{\partial I_c} \right) (C_I)_{cd} \left(\frac{\partial n_b}{\partial I_d} \right), \tag{22}$$

while the covariance error matrix of the polarization vector can be calculated in the following way:

$$C_P = M_P^{H,D} C_N \, (M_P^{H,D})^T. \tag{23}$$

From C_P one can extract the statistical error of the polarization measurement. During normal running conditions, the entire automated procedure to measure and calculate the polarization vectors and their uncertainties lasts roughly 60 s (90 s) for hydrogen (deuterium), resulting in a statistical uncertainty of about ± 0.013 for hydrogen. For deuterium the statistical uncertainty is about ± 0.031 for positive and ± 0.022 for negative nuclear polarization. After an optimization of the BRP sextupole system, and an increase in the diameter of the sample tube, the statistical error of a 60 s measurement is less than 0.5 %.

3.4 The BRP calibration

In the previous section it has been shown that the atomic polarization can be calculated from the measured BRP signals assuming the knowledge of the measurement matrix M_{ia}. This includes the efficiencies of the transition units and the transmission probabilities of the sextupole system for different hyperfine states. The procedure used to determine these parameters is called BRP calibration.
The basic idea of the calibration measurement is to make the system of equations (13) overdetermined so that additional parameters like efficiencies or sextuple transmissions can be extracted through a fit to the data. Due to the fact that the transtion units can be combined in several possible ways, the amount of signals which can be collected during a polarization measurement exceeds the number of hyperfine states N_{hfs}. Yet, the number of unknowns which can be determined in this way is still less than the total number of parameters. The problem can be overcome by cycling this measurement through different (total number N_{ABS}) injection modes (see Tab. 2) so that an adequate number of signals can be collected.

3.4.1 The transition efficiencies

The BRP contains two transition units, a strong field (SFT) and a medium field (MFT) one. The SFT can drive two transitions for hydrogen ($|\,1\,\rangle \leftrightarrow |\,4\,\rangle$ and $|\,2\,\rangle \leftrightarrow |\,4\,\rangle$) and five for deuterium. The efficiencies of the SFT transitions in case of hydrogen are called ε_{s14} and ε_{s24}. The MFT is a multiplestep transition unit which can drive two sub-transitions for hydrogen ($|\,1\,\rangle \leftrightarrow |\,2\,\rangle$ and

BRP-Signal	Name	MFT-RF	MFT	SFT-RF	SFT
OFF	off	OFF	OFF	OFF	OFF
SFT 1-4	s14	OFF	OFF	ON	1-4
SFT 2-4	s24	OFF	OFF	ON	2-4
MFT 1-3	m13c14	ON	1-3	OFF	1-4
MFT 1-3	m13c24	ON	1-3	OFF	2-4
MFT 2-3	m23c14	ON	2-3	OFF	1-4
MFT 2-3	m23c24	ON	2-3	OFF	2-4
MFT 1-3/SFT 1-4	m13s14	ON	1-3	ON	1-4
MFT 1-3/SFT 2-4	m13s24	ON	1-3	ON	2-4
MFT 2-3/SFT 1-4	m23s14	ON	2-3	ON	1-4
MFT 2-3/SFT 2-4	m23s24	ON	2-3	ON	2-4

Table 4
Possible switching modes of the BRP transition units for hydrogen running. During a calibration measurement all signals are collected, while for a polarization measurement only a subset of them is chosen.

$|2\rangle \leftrightarrow |3\rangle$ [8]) and three for deuterium. For hydrogen the MFT is tuned either as a $|1\rangle \leftrightarrow |3\rangle$ (which is achieved by applying the $|1\rangle \leftrightarrow |2\rangle$ and $|2\rangle \leftrightarrow |3\rangle$ transitions sequentially) or as a $|2\rangle \leftrightarrow |3\rangle$ only. In the latter case the MFT unit is tuned to avoid the $|1\rangle \leftrightarrow |2\rangle$ sub-transition. Although nearly zero, the residual $|1\rangle \leftrightarrow |2\rangle$ efficiency for the $|2\rangle \leftrightarrow |3\rangle$ tune of the MFT has to be taken into account.

Due to the limited space available for the BRP equipment, there is a cross talk between the two BRP transition units when both static fields are switched on, so that the tuning of the MFT is influenced by the SFT field, whereas the SFT is not influenced by the (low) MFT field. The MFT efficiencies have to be measured separately depending on the SFT setting, as they depend on the exact static field. This leads, for hydrogen, to an increase in the number of MFT efficiencies from four to eight. The different MFT efficiencies are identified by means of the subscripts $C14$ (for SFT 1-4 static field on) or $C24$ (SFT 2-4 static field on) and by the subscripts r13 or r23 which indicate the particular sub-transition being considered. For example, the notation $\varepsilon_{m13r23c24}$ represents the efficiency of the transition MFT 1-3, step 2-3, tuned together with the static field of the SFT 2-4.
The total number of efficiencies N_{eff} is 10 for hydrogen and 41 in case of

[8] The order of the sub-transitions depends on the sign of the gradient field which is, in the HERMES BRP, negative [16].

deuterium. The number N_{BRP} of possible BRP signals related to different transition states is 11 for hydrogen (as shown in Tab. 4) and 29 for deuterium. If the ABS is operated in N_{ABS} different injection modes, and the BRP transition units switch through all possible N_{BRP} states, the total number of collected signals is $N_s = N_{ABS}\, N_{BRP}$. In this way, recalling Eq. (13), one obtains a system of N_s equations containing $N_u = N_{eff} + N_{ABS}\, N_{hfs}$ unknowns [9], where $N_{hfs} = 4\,(6)$ in case of hydrogen (deuterium). The system can be solved if $N_f = N_s - N_u \geq 0$, where N_f is counting the degrees of freedom and is given by

$$N_f = N_s - N_u = (N_{BRP} - N_{hfs})\, N_{ABS} - N_{eff}. \tag{24}$$

In such a case, both the hyperfine state intensities I_a and the transition efficiencies ε can be determined. For hydrogen, the calibration measurement makes use of 7 ABS injection modes, resulting in $N_f = 39$. In case of deuterium two possible options have been developed, one with 5 ABS modes ($N_f = 74$) and the other with 6 ($N_f = 97$).
The solution of the system is carried out by applying a Runge-Kutta method as explained in [11]. The resulting covariance matrix C_x has the form

$$C_x = \begin{pmatrix} C_\varepsilon & C_{\varepsilon,I} \\ C_{I,\varepsilon} & C_I \end{pmatrix}, \tag{25}$$

where C_ε contains uncertainties and covariances of the efficiencies and is used to calculate the systematic uncertainty of the polarization measurement. The resulting systematic uncertainty induced by the determination of the transition efficiencies of the order of 1.5 %.
Tab. 5 summarizes the transition efficiency measurements performed in 1997 with hydrogen. The efficiencies of the transitions for deuterium running can be found in Ref. [11].

3.4.2 The sextupole transmissions

In the previous section it has been shown how the efficiencies ε_i of the BRP transition can be measured, assuming a priori knowledge of the sextupole transmissions σ_n for different hyperfine states. The attempt to fit both ε_i and σ_n within the same algorithm fails. Nevertheless, the transmission probabilities can be determined by splitting the fitting procedure in two steps, as shown below.
In the BRP setup (Fig. 10), atoms with $m_S = -\frac{1}{2}$ are either defocused or

[9] During the evaluation of the transition efficiencies, the sextuple system transmissions probabilities are assumed to be constant.

Name	MFT	SFT	Efficiency (%)	Error (%)
ε_{s14}	-	1-4	99.3	1.34
ε_{s24}	-	2-4	101.0	1.03
$\varepsilon_{m13r12c14}$	1-3	1-4	101.0	1.03
$\varepsilon_{m13r23c14}$			98.6	1.41
$\varepsilon_{m23r12c14}$	2-3	1-4	-1.0	1.13
$\varepsilon_{m23r23c14}$			94.9	1.23
$\varepsilon_{m13r12c24}$	1-3	2-4	99.9	0.42
$\varepsilon_{m13r23c24}$			90.3	0.82
$\varepsilon_{m23r12c24}$	2-3	2-4	0.0	1.10
$\varepsilon_{m23r23c24}$			97.4	1.04

Table 5
BRP transition unit efficiencies measured during the 1997 hydrogen running fixing the sextupole transmission ratio to $r_{21} = 1.029$. Each efficiency is shown along with an explanation of the MFT and SFT static field setting.

stopped by the beam blocker, having therefore zero transmission probability ($\sigma_3 = \sigma_4 = 0$ for hydrogen and $\sigma_4 = \sigma_5 = \sigma_6 = 0$ for deuterium). Moreover, due to the normalization (Eq. 16), only ratios of transmission probabilities are required for measuring the hyperfine populations. Thus, the remaining required parameters are σ_2/σ_1 for hydrogen and σ_2/σ_1 and σ_3/σ_1 for deuterium.

The Stern-Gerlach force of the sextupole magnets is weaker for hydrogen atoms in state $|\,2\,\rangle$ compared to state $|\,1\,\rangle$ for magnetic fields B of the order or less than the hydrogen critical field $B_c = 50.7$ mT, near the axis of the sextupole system. Thus near-axis atoms in hyperfine states $|\,1\,\rangle$ and $|\,2\,\rangle$ will experience a different transmission efficiency and the transmission ratio $r_{12} = \sigma_1/\sigma_2$ is expected to exceed unity by a small amount. Due to the smaller hyperfine coupling of deuterium, $B_c = 11.7$ mT, the deviation from unity of the ratio σ_2/σ_1 and σ_3/σ_4, is expected to be significantly smaller than for hydrogen. Ray tracing calculations [8] show that the deviation is in fact negligible. From these consideration it follows that the only transmission ratio that needs to be measured is $r_{21} = \sigma_2/\sigma_1$ for hydrogen.
From the BRP calibration the transition efficiencies are extracted as function of the parameter r_{21}. The transmission ratio can thus be evaluated by minimizing the χ^2 of the calibration results. As the transmission probability of the sextupole system depends on the velocity distribution of the atomic sample, the storage cell temperature T_{cell} has to stay constant over the calibration measurement. This procedure applied to a calibration measurement taken at

T_{cell} =95 K has produced the following result [11]:

$$\frac{\sigma_2}{\sigma_1}\Big|_{95\,K} = 1.029 \pm 0.0015 \tag{26}$$

The small error of the measured ratio is neglected in the calculation of the systematic uncertainty of the polarization measurement.
The potential cell temperature dependence of the transition efficiencies can be neglected as the velocity distribution of the sample is fixed by the BRP sextupole system. Therefore, a polarization measurement performed collecting at least one signal more than the minimum required number (as is always the case) can be used to fit the ratio r_{21} for different cell temperatures.

A more detailed description of the BRP calibration and performance can be found in Ref. [11].

4 Processes occurring inside the Storage Cell

Inside the storage cell, the atoms of the target may experience several interactions which have an influence on the average target polarization P^T. Their complete understanding is therefore fundamental for the reduction of the systematic error of the target polarization. In this section an overview of the different processes will be given, while a quantitative estimation of the various contributions for the different running periods of the HERMES target can be found in Sec. 6. The processes are divided into two categories:

- Recombination processes.
  - · Surface recombination;
  - · Effect on nuclear spin.

and

- Spin relaxation processes:
  - · Wall collisions
  - · Spin exchange collisions
  - · Resonant interaction of HERA beam and the spins of the target gas

Recombination and relaxation by wall collisions are surface effects whereas spin exchange collisions and resonant interaction of beam and target gas happen in the gas storage cell volume. The experimental conditions of the target are chosen such that these unwanted effects are suppressed as much as possible. It should be noted that spin relaxation can be studied and monitored with good statistics by means of BRP, whereas the reasidual polarization after

recombination can only be studied using scattering process like deep inelastic scattering (DIS) with very low rate.

4.1 Recombination Processes

The atoms which are injected into the HERMES target storage cell may recombine to molecules keeping partly their nuclear polarization or not. Recombination [12] can in principle take place either on the storage cell walls (surface recombination) or in the gas phase (volume recombination). At the low gaseous densities of the HERMES target volume recombination is negligible. On the cell walls two types of processes with surface catalysis of recombination can be distinguished which are expected to result in different residual nuclear polarization:

- the Langmuir-Hinselwood (L-H) process, where the two adsorbed, thermalized atoms react with each other;
- the Eley-Rideal (E-R) process, where an atom from the gas phase reacts directly with an absorbed atom [25].

The residual polarization of the surface atoms recombining through the E-R mechanism in the cell has been measured with the HERMES spectrometer, making use of a well known asymmetry DIS. The result has been presented in Ref. [14] and it will be discussed in section 5.2.

Since the storage cell temperature usually is kept below 140 K, a small amount of water originating from the dissociation in the atomic beam source freezes on the surface and grows into an ice layer on top of the Drifilm surface. The presence of water is important since water is known to inhibit hydrogen or deuterium recombination. The most likely reason for this is that the chemical binding energy of an hydrogen atom in water (H-OH) of 498 kJmol^{-1} is higher than in a hydrogen molecule (435.99 kJ/mol). The same applies for the case of deuterium, where the bond strength of D-OD is higher than the one of D-D bonds. New storage cell coatings are hydrophobic and the growth of the ice layer is affected by the continuous irradiation of the storage cell surface by the HERA beam which changes the chemical structure of the surface causing the surface to become less hydrophobic In addition, synchrotron photons cause water molecules to desorb from the cell wall. Thus ice coverage of the cell surface is determined by the radiation dose collected by the surface coating. It has been observed that during the running the amount of recombination in the cell gradually decreases thanks to the water effect.

A detailed description of the recombination studies performed on the HERMES storage cell can be found in Ref. [12].

4.2 Spin relaxation

Three different spin relaxation mechanisms of atoms can in principle be observed to occur in the HERMES target as they cause a change in the hyperfine population inside the storage cell. One relaxation process takes place on the wall of the storage cell. Another is due to two-body spin-exchange collisions of atoms in the gas phase. In the third mechanism the high frequency field associated with the HERA beam can cause a depolarization in the target atoms under certain conditions [13]. Spin relaxation of atomic hydrogen by wall or spin exchange collisions with different types of wall coatings has been under study already for many years in the context of a hydrogen maser for low holding fields [6]. For the HERMES target further studies of the magnetic field dependence of spin relaxation as well as studies of the temperature dependence and of the density dependence of the transition spectra have been carried out [16,30–33]. The results of these studies are summarized in the following sections.

4.2.1 Wall relaxation

The atoms injected by the atomic beam source experience some hundreds of wall collisions during their diffusion process through the storage cell. An attractive Van-der-Waals potential between the storage cell wall and a diffusing atom causes the atom to be physisorbed, i.e. to stay for a certain time close to the surface until it is desorbed again. The mean residence time on the wall τ_s is described by the Arrhenius equation:

$$\tau_s = \tau_0 \, e^{\left(\frac{E_b}{kT}\right)}, \tag{27}$$

where τ_0 is the high temperature limit of τ_s, E_b and T are the adsorption energy and temperature respectively, and k is the Boltzmann constant. During the time an adsorbed atom stays on the wall ($\approx 10^{-10}$ s for the HERMES cell), the magnetic moment of its unpaired electron interacts with magnetic moments on the surface by means of a dipolar coupling and/or with other unpaired electrons through exchange interaction [18–21].

Depending on the surface type, temperature and magnetic field one can define a probability that the atom leaves the wall in a certain hyperfine state. This is described by means of transition probabilities W_{jk} which represents the probability to find an atom in state $|\,k\,\rangle$ that has been in state $|\,j\,\rangle$ prior to the wall collision.

The theoretical description and calculation of the transition probability matrix for the HERMES target can be found in [16].

4.2.2 Spin Exchange Depolarization

Atoms colliding with each other in the gas phase can undergo spin exchange, where the hyperfine states can be modified via interaction between the electron spins [34]. Due to the conservation of angular momentum, the sum of the magnetic quantum numbers m_F before and after the spin exchange collision has to be the same:

$$\Delta \sum_i m_F = 0. \tag{28}$$

One can see that if an initial population of the gas consists only of pure states $|\,1\,\rangle$ or $|\,3\,\rangle$ in case of hydrogen and $|\,1\,\rangle$ or $|\,4\,\rangle$ in case of deuterium, no relaxation by means of spin exchange is possible. This is actually not the case of the HERMES cell, where to double the density, a mixture of pure and mixed states is injected during the data taking. The effect of spin exchange collisions on the hyperfine populations can be described by a tensor M^k_{jk}, which gives the probability to find an atom in state $|\,i\,\rangle$ after a collision of two atoms in the state $|\,j\,\rangle$ and $|\,k\,\rangle$ prior to the collision:

$$\frac{dN_i}{dt} \propto \sum_{j,k} M^i_{jk} \tag{29}$$

The number of spin exchange collisions per unit time and volume is

$$\dot{N}_{se} = n\sigma_{se} \langle\, v_r \,\rangle\,, \tag{30}$$

where n is the gas density, σ_{se} is the spin exchange cross section and v_r is the relative velocity of the atoms. The density dependence of spin-exchange collision relaxation, combined with the knowledge of σ_{se} [35,36], has been used to determine the density inside the HERMES cell [16], the results will be reported in Sec. 6.

4.2.3 Master equation for the description of the spin relaxation process

The different relaxations due to wall collisions and spin exchange collisions cannot be treated separately. After the interaction with the surface during a wall collision the atom in the gaseous phase, interacts through spin exchange collision and, at the next wall collision, interacts again with the surface. Since the atoms are constantly exposed to both interactions, an appropriate description is given by so called *master equation* for the occupation numbers N_i of

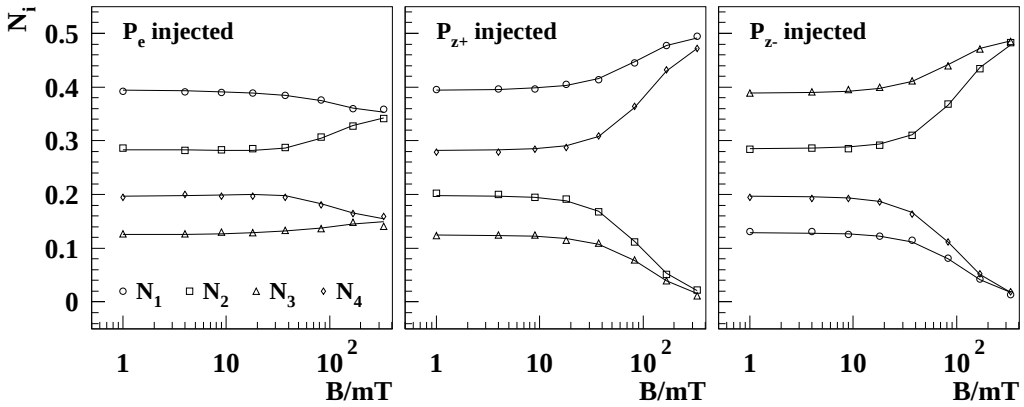

Fig. 11. Measured hyperfine population vs. magnetic field for hydrogen for the different injection modes. The measured values are given by symbols, while the lines show a fit using the solutions of Eq.31

the hyperfine state $|\, i \,\rangle$ [16,30]:

$$\frac{dN_i}{dt} = \frac{1}{\tau_d}(N_i^{inj} - N_i) + \frac{\tau_d}{\tau_f}\sum_k W_{jk}N_k + \frac{\tau_d}{\tau_{se}}\sum_{jk} M_{jk}^i N_j N_k \qquad (31)$$

The first part of Eq. 31 represents the incoming outgoing flux, the third the wall relaxation and the last term the spin exchange relaxation. The effect of recombination is not included in this formula.

In Eq. 31 three time constants appear: τ_d (the diffusion time) is the mean occupation time of atoms within the storage cell, τ_f is the mean time of flight between two wall collisions and τ_{se} is the mean time between two spin exchange collisions. For times that are large compared to τ_d the hyperfine population converges toward a dynamical equilibrium (*steady state*). The steady state population is of practical interest, because the BRP requires a stable hyperfine population for a polarization measurement.

The solution of the linear algebric equation system 31 in the steady state has been solved directly in the case of hydrogen or with the help of a numerical iteration algorithm in the case of deuterium [16].

As an example of application of Eq. 31, Fig. 11 represents the measured hyperfine population as a function of the magnetic field for hydrogen and a fit to the data using the solutions of Eq. 31.

4.2.4 Bunch field induced depolarization

The beam current of the HERA electron storage ring is bunched with time τ_{bunch} between two adjacent bunches of 96.1 ns. Typically, most of the 220 RF

buckets are filled, so that the bunch frequency is given by:

$$\nu_{bunch} = \frac{1}{\tau_{bunch}} = 10.42 MHz. \tag{32}$$

A large number of harmonics contributes to the induced magnetic high frequency field close to the HERA beam, because the bunches are very short. The transition frequency between two hyperfine states $|\, i \,\rangle$ and $|\, j \,\rangle$ is given by:

$$\nu_{ij} = \frac{E_i(B) - E_j(B)}{h}. \tag{33}$$

If at a certain holding field B ν_{ij} matches one of these harmonics, resonant depolarization occurs. The location of the beam-induced resonances is shown in Fig. 12. Bunch field induced depolarization at the HERMES target have been studied in case of hydrogen [13,33] and deuterium [16] for the longitudinal orientation of the target holding field (before 2001). During this time the observed π ($\Delta m = \pm 1$) transitions were sufficiently separated so that at the working point (335 mT) no beam induced depolarization could be found. In the case of transverse target operating since October 2001, both σ ($\Delta m = 0$) and π ($\Delta m = \pm 1$) transitions are allowed because the oscillating field surrounding the HERA beam has components both parallel and perpendicular to the static holding field. The spacing between two nearby induced resonances is narrower than in the longitudinal case (only 0.37 mT difference in the magnetic holding field at B = 0.3 T) and a higher homogeneity in the holding field is therefore needed (see Fig. 12).

Thus, a field intensity for which beam resonant depolarization can be completely suppressed does not exist. A pair of additional correction coils mounted directly near the storage cell has been installed for the 2003 running. The results will be presented in a forthcoming paper.

5 Target polarization

The average polarization of the nucleons in the target P^T is a fundamental parameter of the HERMES experiment. The problem is to relate the measured polarization of the atoms in the sample beam with the density-weighted average polarization of the nuclei in the cell. The definition of the target polarization involves different terms which mainly account for two effects:

- Presence of molecules in the cell, both unpolarized from the residual gas of the scattering chamber and/or directly injected from the ABS, and polarized

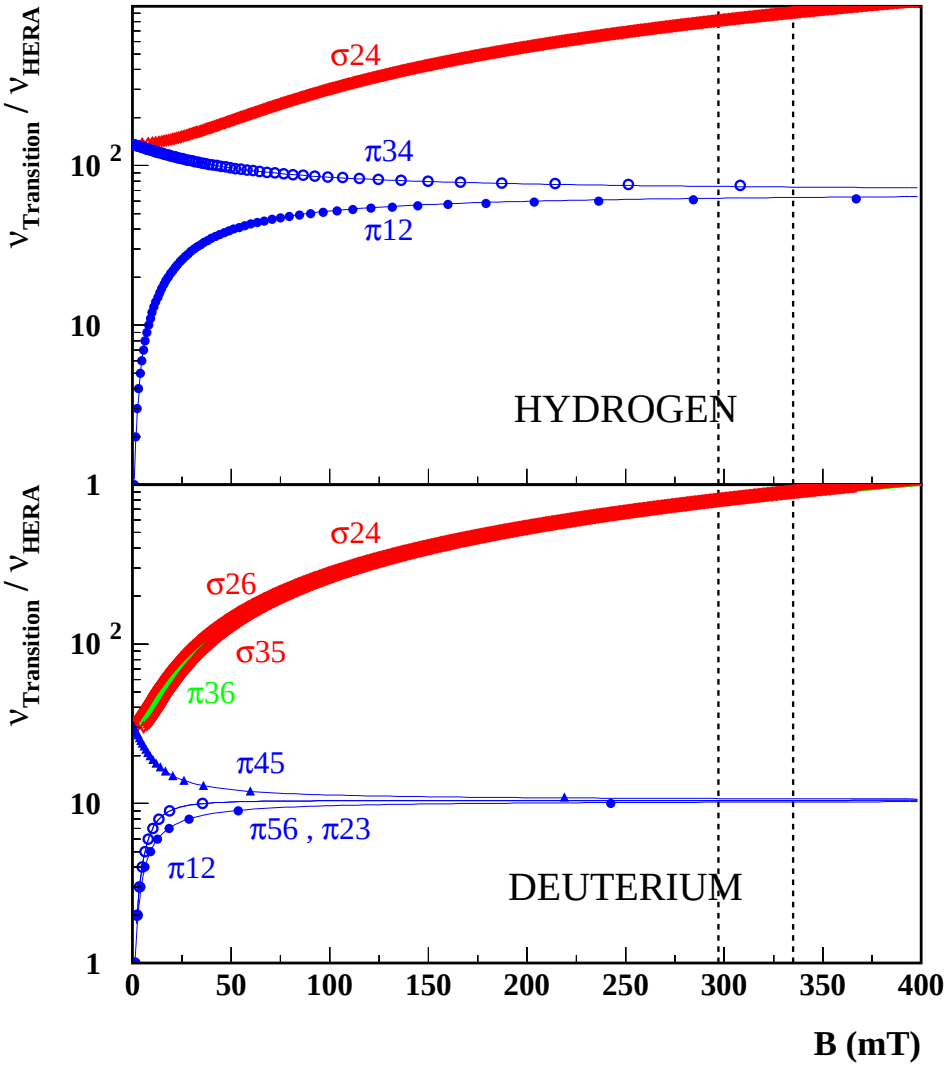

Fig. 12. Possible beam induced nuclear depolarizing resonances in the HERMES target. The frequency difference between pairs of hyperfine states whose transitions lead to nuclear depolarization are plotted as a function of the holding field. The frequency values are normalized to $\nu_{HERA} = 10.42\,\mathrm{MHz}$. The symbols, representing the resonance condition, are clearly distinguishable for the π transitions, while they overlap with each other in case of σ and $\pi\,|\,3\,\rangle \leftrightarrow |\,6\,\rangle$ transitions, which are separated by a difference in the intensity of the holding field ΔB_T of only 0.37 mT. The dashed lines represent the working point of the transversely (left) and longitudinally (right) polarized targets.

coming from recombination of polarized atoms on the cell surface.

- Relaxation and recombination effects in the storage cell leading to an inhomogeneous distribution of the atomic fraction and of the atomic polarization.

The average target polarization P^T as seen by the electron beam is defined by the following equation:

$$P^T = \alpha_0 \alpha_r P_a + \alpha_0 (1 - \alpha_r) \beta P_a, \tag{34}$$

where α_0 represents the initial fraction of nucleons in atoms as injected by the ABS (or atomic fraction in absence of recombination), α_r denotes the fraction of nucleons in atoms surviving recombination during their way through the storage cell, $\beta = P_m/Pa$ stands for the ratio of the polarization of the molecules produced by recombination P_m relative to the polarization of the atoms P_a. The knowledge of β for the experimental conditions at the HERMES experiment will be discussed in Sec. 5.2.

The values for α_0, α_r and P_a are calculated using the measurements of the TGA and BRP combined with the various calibrations. As both detectors measure the properties of a sample of the target gas, it is necessary to relate the results to a corresponding value averaged along the storage cell. This is achieved by the sampling corrections c_α [15]:

$$\alpha_r = c_\alpha \alpha_r^{TGA} \tag{35}$$

and c_P

$$P_a = c_P P_a^{BRP} \tag{36}$$

The sampling corrections and their systematic uncertainties are functions of the measured values of α_r^{TGA} and P_a^{BRP}, respectively. The functions depend on the geometry of the storage cell, its surface properties and the detectors acceptance. They are calculated with the help of Monte Carlo simulations of the stocastic motion of particles in the storage cell, where the history of these particles is stored and analyzed. Another possibility is to calculate sampling corrections analytically by describing the diffusion process of the target gas inside the storage cell with the use of a one-dimensional diffusion equation. The issue has been addressed in Ref. [15] and will be discussed here in Sec. 5.4.

The different terms entering the definition of the average polarization are summarized in Tab. 6.

Term		Meaning
P^T		density averaged polarization in the cell
α_0		atomic fraction in the absence of recombination within the cell
α_r	$= c_\alpha \alpha_r^{TGA}$	fraction of atoms surviving recombination in the cell
	c_α	sampling correction for the atomic fraction
	α_r^{TGA}	measured atomic fraction in the sample beam
$(1-\alpha_r)$		fraction of atoms recombining in the cell
P_a	$= c_P P_a^{BRP}$	polarization of atoms in the cell
	c_P	sampling correction for the atomic polarization
	P_a^{BRP}	measured polarization of atoms in the sample beam
β	$= P_m/P_a$	relative nuclear polarization of recombined atoms

Table 6
Meaning of the different terms contained in Eq. 34.

5.1 Determination of the quantities α_r and α_0

In order to calculate the target polarization following Eq. 34, it is necessary to separate the atomic fraction that would be seen by the HERA electron beam if no cell wall recombination were to occur (α_0), and the fraction of the initially injected atoms that survive wall recombination, as seen by the HERA electron beam (α_r). The measured quantity α^{TGA} can also be factorized in two terms and can be written as (see Eq. 9):

$$\alpha^{TGA} = \frac{\phi_a}{\phi_a + \phi_m} = \alpha_0^{TGA} \alpha_r^{TGA} \tag{37}$$

As long as dissociative ionization can be neglected the only source of atomic flux ϕ_a into the gas analyzer is the flux originating from the atomic beam source. The molecular flux ϕ_m on the contrary may come from three different sources:

- Undissociated molecules ballistically injected by the ABS. Since the efficiency of the dissociator is around 80 %, a certain amount of molecules passes through the nozzle towards the polarizing stage, affected by neither the sextupole magnets or the transition units. Although the majority of these molecules hits the vacuum chamber wall and is pumped away, a small amount enters into the storage cell via the injection tube. These unpolarized molecules present a triangular density distribution along the cell axis, with the maximum density at the center of the cell.
- Rest gas in the target chamber. These molecules mainly originate from the

recombination of atoms that have left the storage cell and have thermalized on the vacuum chamber walls. This molecular component is clearly unpolarized and results in a constant density inside the storage cell.

- Atoms that recombine into molecules after entering the cell. As explained in section 2.3, the cell material and temperature are optimized in order to limit the depolarization and recombination effects in the target atomic gas. Nevertheless, atoms can stick on the cell surface and recombine and the resulting molecules may carry a residual nuclear polarization.

Hence, the normalized total molecular flow rate ϕ_m can be decomposed in the following way:

$$\phi_m = \phi_{bal} + \phi_{rg} + \phi_r \tag{38}$$

where ϕ_{bal}, ϕ_{rg} and ϕ_r represent the ballistic, the rest gas and the recombination components, respectively.

To separate between polarized and unpolarized molecules we rewrite the two factors in Eq. 37 by using the different contributions defined in Eq. 38:

$$\alpha_r^{TGA} = \frac{\phi_a}{\phi_a + \phi_r}, \tag{39}$$

and

$$\alpha_0^{TGA} = \frac{\phi_a + \phi_r}{\phi_a + \phi_r + \phi_{bal} + \phi_{rg}}. \tag{40}$$

The separation of the total molecular flowrate into the single components is accomplished by means of standard *target calibrations* which are usually performed between two HERA electron fills, when the HERMES spectrometer is not taking data.

The rest gas contribution (ϕ_{rg}) to the molecular flux is linearly proportional to the pressure in the target chamber. The constant of proportionality is determined by injecting into the target chamber increasing quantities of hydrogen (deuterium) molecules with a controlled flow system and by measuring the corresponding TGA count rates.

The ballistic flux contribution (ϕ_{bal}) can be measured by varying the atomic flux of the injected beam while keeping the molecular flux constant. The atomic flux is changed by using the hyperfine transitions to select either 1 or 2 (or 3 in the case of deuterium) hyperfine states. Since the recombination probability inside the cell is independent of the injected beam intensity, the

quantity ϕ_{bal} can be extracted. Equation 38 is then solved for the remaining molecular flux ϕ_r.

A detailed description of how these calibrations are performed has been given in Ref. [10].

Once the molecular contributions ϕ_{rg}, ϕ_{bal} and ϕ_r are extracted one can determine α_r^{TGA} using Eq. 39 and thus α_r using Eq. 35.

The term α_0 can be determined without referring to additional sampling corrections. It should be noted that all the ϕ_i terms in Eq. 40 are nucleon fluxes, but α_0 is related to nucleon densities in the cell as seen by the HERA beam. In the limiting case of small cell wall recombination, the densities of atoms and molecules arising from ϕ_a, ϕ_{bal} and ϕ_r are triangular. In contrast, the rest gas ϕ_{rg} has a constant density along the cell and must be weighted by another factor of 2. Additionally, ϕ_{bal} and ϕ_{rg}, having double atomic mass, represent a target thicker by a factor $\sqrt{2}$ for the same TGA flux then atoms. Finally, the terms ϕ_a and ϕ_r are coupled. An increase in ϕ_r is offset by a decrease in ϕ_a so that $\phi_a + \phi_r =$ constant. Nevertheless the target density from the nucleons depends on α_r according the term $d = \sqrt{2}/(1 + (\sqrt{2} - 1)\alpha_r)$. Combining the above considerations gives:

$$\alpha_0 = \frac{d(\phi_a + \phi_r)}{d(\phi_a + \phi_r) + \sqrt{2}\phi_{bal} + 2\sqrt{2}\phi_{rg}}. \tag{41}$$

5.2 Relative polarization of nuclei in recombined atoms (β)

As mentioned in the previous sections, a certain amount of polarized hydrogen or deuterium atoms may recombine in the storage cell. A direct measurement of the remnant polarization contained in the molecules is not possible at HERMES, as the Breit-Rabi polarimeter can measure the atomic polarization only. The atomic recombination is a temperature dependent surface mediated process [12,16]. Hence, measurements of the nuclear polarization of recombined atoms using storage cells of different materials and/or with different coatings [37,38] are not directly applicable to the HERMES case. Without any information about the molecular polarization β of nucleons in molecules (or molecular polarization in short) one has to apply in Eq. 34 the conservative assumption $0 \leq \beta \leq 1$. Recently, a set of data taken in 1997 at warmer cell temperature (260 K instead of the nominal 100 K) could be used to measure β for hydrogen at that temperature, resulting in: $\beta^{260K} = 0.68 \pm 0.09_{stat} \pm 0.06_{syst}$ [14]. This result can be used as an upper limit for β at 100 K (β_{high}^{100K}) under the following assumptions. The main mechanism responsible for recombination at 100 K and 260 K is the same (i.e. the E-R mechanism). At 100 K, the recombination probability is smaller than at 260 K (the atoms impinging from

the volume have less kinetic energy to overcome the activation barrier). Thus, the residence time of chemically adsorbed atoms on the surface at 100 K is greater than at 260 K and their possible polarization cannot exceed the value measured at 260 K. This results in $\beta_{high}^{100K} = 0.83$.

The lower limit for β^{100K} (β_{low}^{100K} can be derived from a simple argument. By assuming that the nucleon spins are not affected by the recombination process, the nuclear polarization of the molecule at its formation (P_m^0) can be evaluated by taking the average value of the polarization of an atom coming from the volume (P_a) and one resident on the surface (P_s). The theoretical lower limit for β^{100K} can then be inferred supposing that atoms sticking on the cell surface are totally depolarized ($P_s^{100K,low} = 0$) and applying the equation:

$$\beta_{low}^{100K} = \frac{P_m^{100K,low}}{P_a^{100K}} = \frac{P_a^{100K} + P_s^{100K,low}}{2} \frac{1}{P_a^{100K}}. \tag{42}$$

The result is $\beta_{low}^{100K} = 0.5$. A factor of 0.9 takes the collisional depolarization of the molecules on the walls into account [14,38], ending in $\beta_{low}^{100K} = 0.45$.

Hence, the range of β^{100K} can be limited to

$$0.45 \leq \beta^{100K} \leq 0.83. \tag{43}$$

The final value and error of β^{100K} is:

$$\beta^{100K} = 0.64 \pm 0.19 \tag{44}$$

5.3 Injected atomic polarization

An important parameter for the exact evaluation of the target polarization is the injected atomic polarization P_a^{inj} (i.e. the atomic polarization in absence of depolarization), as it enables the decoupling of the different spin-relaxation effects. The injected polarization for each ABS operating mode (Tab. 2) can be calculated if the transmission probabilities of the sextupole system and the efficiencies of the adiabatic transition units are known. The sextupole transmission probabilities for hydrogen and deuterium have been calculated using a Monte Carlo simulation and the results are given in Ref. [8]. The efficiencies of the transitions of the ABS can be extracted by measuring the magnetic field dependence of the spin relaxation processes and by fitting the data with a theoretical model referred to as *'master equation'* which is described in Ref. [16].
For the HERMES data, the important ABS injection modes are those (two hyperfine states) having a large positive or negative nuclear polarization, P_{z+}

and P_{z-} respectively, and, in case of deuterium, the two additional positive and negative tensor polarization (P_{zz+} and P_{zz-}) modes (see Tab. 2).

For hydrogen, only two transitions after the sextupole system are used: the SFT 2-4 for P_{z+} and WFT 1-3 for P_{z-}. Therefore, the injected polarizations are directly given by the transition efficiencies whose values have been calculated in Ref. [16] using the technique mentioned and cross-checked using a more direct method based on the symmetry of the spin relaxation processes for the two injection modes. In case of deuterium, several transition units are used to provide the four polarizations, some of which are located between the two sextupole subsystems. Hence, the injected polarizations have to be calculated taking into account the transition efficiencies as well as the transmission probabilities for atoms whose hyperfine state gets changed between the two subsystems.
The calculated polarization for the hydrogen and deuterium beams injected into the target are summarized in Tab. 7. The degree of nuclear polarization injected by the ABS when running with deuterium is substantially lower than for hydrogen. The reason is that, due to the higher number of hyperfine states, the deuterium nuclear polarization can only be achieved by using the transition units located between the two magnetic subsystems, resulting in an incomplete separation of states.

5.4 Sampling Corrections

The sampling correction functions $c_\alpha(\alpha_r^{TGA})$ and $c_P(P_a^{BRP})$ depend strongly on the distribution of recombination and wall relaxation probabilities per wall collision along the storage cell. If the storage cell has not yet been exposed to the HERA beam, one can assume that the recombination and wall relaxation probabilities are constant over the entire surface of the storage cell, or, at least, that microscopic inhomogeneities by different types of surface sites

Mode	Hydrogen	Deuterium
P_{z+}^{inj}	97.26 ± 0.05	87.78 ± 0.07
P_{z-}^{inj}	-97.38 ± 0.07	-89.50 ± 0.10
P_{zz+}^{inj}	-	96.22 ± 0.38
P_{zz-}^{inj}	-	-177.30 ± 0.61

Table 7
Estimated polarizations for the hydrogen and deuterium atomic beams injected by the ABS into the target. All values are multiplied by 100. The quoted errors take only the uncertainty of the ABS efficiencies into account. The values refer to the polarization of injected gas with 0.3 T guide field.

are equally distributed. In normal operation no influence of the HERA beam on the target performance has been observed. Nevertheless certain distinct incidents affecting the cell have been found, when the beam tuning was not optimum or the HERA beam was accidentally lost near the HERMES target region. Possible mechanisms how the HERA beam could affect the surface properties of the storage cell might be:

- desorption of surface coating by a synchrotron radiation flash;
- bombardment of the storage cell walls with charged particles leading to radiation damage;
- chemical reactions of ionized hydrogen or deuterium radicals with the cell surface;
- redistribution of the ice layer on the storage cell by RF heating due to the wake fields;
- contamination of the storage cell surface by sputtered material from the collimator upstream of the target.

Since the exact effect of the HERA beam on the surface properties is unknown, every realistic distribution of recombination and wall relaxation probabilities has to be considered when evaluating the sampling corrections. It is anyway convenient to distinguish certain scenarios of special interest.

- **Homogeneous cell (HC):** the natural assumption when the cell has not been exposed to the HERA beam. The calculated sampling corrections set an upper limit for α_r and P_a for any given values of α_r^{TGA} and P_a^{BRP} respectively.
- **Homogeneous beam tube (HBT):** the beam tube is homogeneously affected by the beam, while the side tubes are unaffected.
- **Inhomogeneous beam tube (IBT):** beam tube is inhomogeneously affected by the beam, while the side tubes are unchanged. This scenario does not lead to a single sampling correction, but it can be used to calculate a lower limit for α_r and P_a for any given values of α_r^{TGA} and P_a^{BRP} respectively.

A model for calculating the sampling corrections has been developed in Ref. [16] which is based on a parameter $\gamma_r(\gamma_d)$, the recombination (spin-flip) probability during a wall collision. If these probabilities were constant and equal for the beam and sample tubes, the sampling corrections would only depend on their geometry. This is actually the case for a freshly installed cell, whose Drifilm coating is known to be intact and uniform.

In all scenarios it is assumed that the relation $\gamma_r^{ST} \leq \gamma_r^{BT}$ holds at any time for the recombination probabilities in the sample tube, γ_r^{ST}, and beam tube, γ_r^{BT}. The validity of this hypothesis is proven by the data [16,24]. Numerical calculations of the sampling corrections for the "large cell" have been performed using a molecular flow simulation, complemented by analytical calculations

based on the one-dimensional diffusion equation [16].

The sampling correction c_P has to be subdivided into two different terms, one for the wall collisions and a second one for spin exchange relaxation, as the two processes have to be treated in different ways. This can be done by defining the depolarization factors $\pi_{wd} = 1 - \Delta P_a^{wd}$ (wall collisions) and $\pi_{se} = 1 - \Delta P_a^{se}$ (spin exchange relaxation) so that, for low spin relaxation, one has:

$$\frac{P_a}{P_a^{BRP}} \equiv c_P \simeq \frac{\pi_{wd}\,\pi_{se}\,P_a^{inj}}{\pi_{wd}^{BRP}\,\pi_{se}^{BRP}\,P_a^{inj}} \tag{45}$$

As the spin exchange relaxation occurs in the gas phase, this process is not affected by any change of the cell surface properties, so that the relation between π_{se} and π_{se}^{BRP} has to be independent from any of the listed scenarios. Moreover, since calculations have shown that $\pi_{se} \simeq \pi_{se}^{BRP}$ [16], one can conclude that the sampling correction c_P is determined by the wall depolarization only:

$$c_P = \frac{P_a}{P_a^{BRP}} \simeq \frac{\pi_{wd}}{\pi_{wd}^{BRP}} \tag{46}$$

As an example in Fig. 5.4 the effect of the calculated sampling corrections for the "large cell" used in the 1996-97 running with hydrogen is shown. During data taking the measurements of α_r^{TGA} and π_{wd}^{BRP} are almost always well above 0.9, so that linear approximations for the sampling corrections are used:

$$\alpha_r = \bar{a} + (1 - \bar{a})\,\alpha_r^{TGA} = \alpha_r^{TGA} + \bar{a}\,(1 - \alpha_r^{TGA}) \tag{47}$$

$$\pi_{wd} = \bar{b} + (1 - \bar{b})\,\pi_{wd}^{BRP} = \pi_{wd}^{BRP} + \bar{b}\,(1 - \pi_{wd}^{BRP}) \tag{48}$$

The values $\bar{a}$, for recombination, and $\bar{b}$, for depolarization, are obtained by taking the average between the two extreme scenarios and assigning them systematic errors $\Delta\bar{a}$, $\Delta\bar{b}$ equal to the difference between the average value and the extremes (see the dotted lines in Fig. 5.4).

5.5 Evaluation of the systematic error

After having determined all the single terms of Eq. (34), P^T can be expressed as a function of the measured quantities. It is convenient to write the target

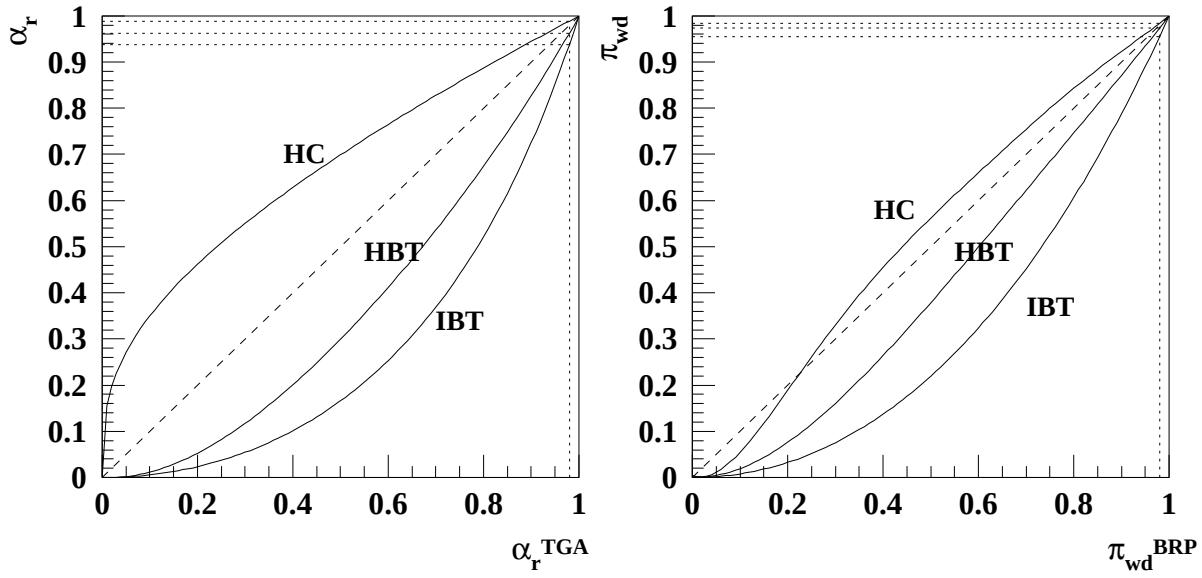

Fig. 13. Correlation between the values measured by the TGA or BRP detectors and their corresponding density weighted average values in the storage cell. The left figure shows the range for recombination, the right picture shows the range for wall depolarization. Acceptable uncertainties of α_r and π_{WD} can only be achieved with α_r^{TGA} and π_{WD}^{BRP} close to unity. The uncertainty grows rapidly with increasing recombination or depolarization respectively.

polarization in the following way:

$$P^T = \alpha_0 \left(\alpha_r + (1 - \alpha_r)\, \beta\right) P_a = \alpha_{tot} \cdot P_a.. \tag{49}$$

where the term α_{tot} is called *effective* atomic fraction.

5.5.1 Error of the effective atomic fraction α_{tot}

Combining equations (49), (47) and (39), α_{tot} can be expressed by

$$\alpha_{tot} = \frac{\phi_a + (\bar{a}\,(1-\beta) + \beta)(\phi_m - \phi_{bal} - \phi_{rg})}{\phi_a + \phi_m + (\sqrt{2}-1)\phi_{bal} + (2\sqrt{2}-1)\phi_{rg}}. \tag{50}$$

The systematic uncertainty of α_{tot} is determined by the measured flow rates ϕ_a, ϕ_m, ϕ_{bal} and ϕ_{rg} and their errors as well as the values and uncertainties of β, $\bar{a}$ and the TGA calibration constant κ. With the matrix T defined by

$$T = \left(\frac{\partial \alpha_{tot}}{\partial \phi_i}, \ldots, \frac{\partial \alpha_{tot}}{\partial \kappa} \right), \tag{51}$$

and the diagonal covariance matrix C of all calibration constants, the systematic uncertainty $\Delta_{sys}\alpha_{tot}$ is given by

$$\Delta_{sys}\alpha_{tot} = \sqrt{TCT^T}. \tag{52}$$

The matrix T contains 10 independent derivatives, i.e. for κ, $\bar{a}$, β and the terms related to the ballistic flux and rest gas calibrations (7 additional terms as described in Ref. [10]).

5.5.2 Error of the atomic polarization P_a

Combining equations (45) and (48), and using the approximation:

$$\pi_{se}^{BRP} \simeq \frac{1}{1+\Delta(P_a^{se})^{BRP}}, \tag{53}$$

the formula for the average atomic polarization P_a can be written in the following way

$$P_a = P_a^{BRP} + \bar{b}\,(\pi_{se}\,P^{inj} - P_a^{BRP}) \simeq P_a^{BRP} + \bar{b}\left(\frac{P^{inj}}{1+\Delta P_a^{se}} - P_a^{BRP}\right). \tag{54}$$

For the calculation of the systematic uncertainty $\Delta_{sys}\,P_a$, the important error sources to be included are $\Delta\bar{b}$ and $\Delta_{sys}\,P_a^{BRP}$ [10]. As a result, one finds:

$$\Delta_{sys}P_a = \left((1-\bar{b})^2(\Delta_{sys}P_a^{BRP})^2 + (1-\pi_{wd})^2\pi_{se}^2(P^{inj})^2\Delta\bar{b}^2\right)^{1/2}. \tag{55}$$

During the analysis one typically averages over a large dataset, so that the statistcal uncertainty of the polarization measurement $\Delta_{sta}\,P_a$ is negligible.

6 Performance

In the present section an overview about the target performance over the total running time will be given by analyzing distinct periods for each different target:

- 1997 for the longitudinal hydrogen target;
- 2000 for the longitudinal deuterium target;
- 2002 for the transverse hydrogen target.

[10] The uncertainties on ΔP_{se} and on P_a^{inj} are negligible.

6.1 Longitudinal hydrogen running in 1997

The upper plot in Fig. 14 shows the atomic fraction α^{TGA} measured by the target gas analyzer during the 1997 running period. The atomic (nuclear) polarization measured by the BRP is plotted in the lower half of Fig. 14. Aside from startup problems, the target performance was relatively smooth. Unfortunately, a severe HERA beam loss close to the HERMES region occurred at a certain point (left line), resulting in a change of the cell surface properties. After this bad event, it was decided to collect a set of data at higher temperature ($T_{cell} = 260\,\mathrm{K}$ instead of the nominal value $T_{cell} = 100\,\mathrm{K}$) in order to measure the β parameter (see Ref. [14]). At the end of this period, the storage cell was exchanged (middle line). Also the second cell experienced a beam dump (right line) which produced a small hole in the cell wall.
For these reasons during the analysis, the 1997 dataset has been divided into four periods during which the cell surface condition was assumed to be constant. For each period, specific studies have been performed to limit the errors on α_r and P_a [24].

For the entire running period with hydrogen, we quote a luminosity-weighted average value for the target polarization of $P^T_{z+} = -P^T_{z-} = 0.852 \pm 0.033$ and a density of 7.6×10^{13} nucl./cm^2 . The latter number has been derived from a method exploiting the density dependence of spin exchange collisions [16].

6.2 Longitudinal deuterium running in 2000

Over the eight month of deuterium running in 2000, the HERMES target operated in very stable conditions. The atomic beam source, equipped with a microwave dissociator, experienced only one major failure which hardly affected the data taking. Neither the scattering chamber, nor the TGA/BRP vacuum system had to be opened, leading to constant amounts of residual gas in the storage cell as well as stable efficiencies of the detectors of the target diagnostics. There was no need to replaced the storage cell, as its performance in terms of atomic recombination and nuclear depolarization was always excellent. The reason for such good behavior can be found both in a particularly fortunate Drifilm coating and in the limited damage caused by a very well tuned electron beam.

The outstanding performance of the HERMES target in this period is well represented in Fig. 15 (note the change in scale compared to Fig. 14). The stable behavior of the cell surface in terms of atomic recombination is demonstrated in the upper plot of Fig. 15, where the atomic fraction measured by the target gas analyzer is plotted. The lower plot shows the nuclear polarization.

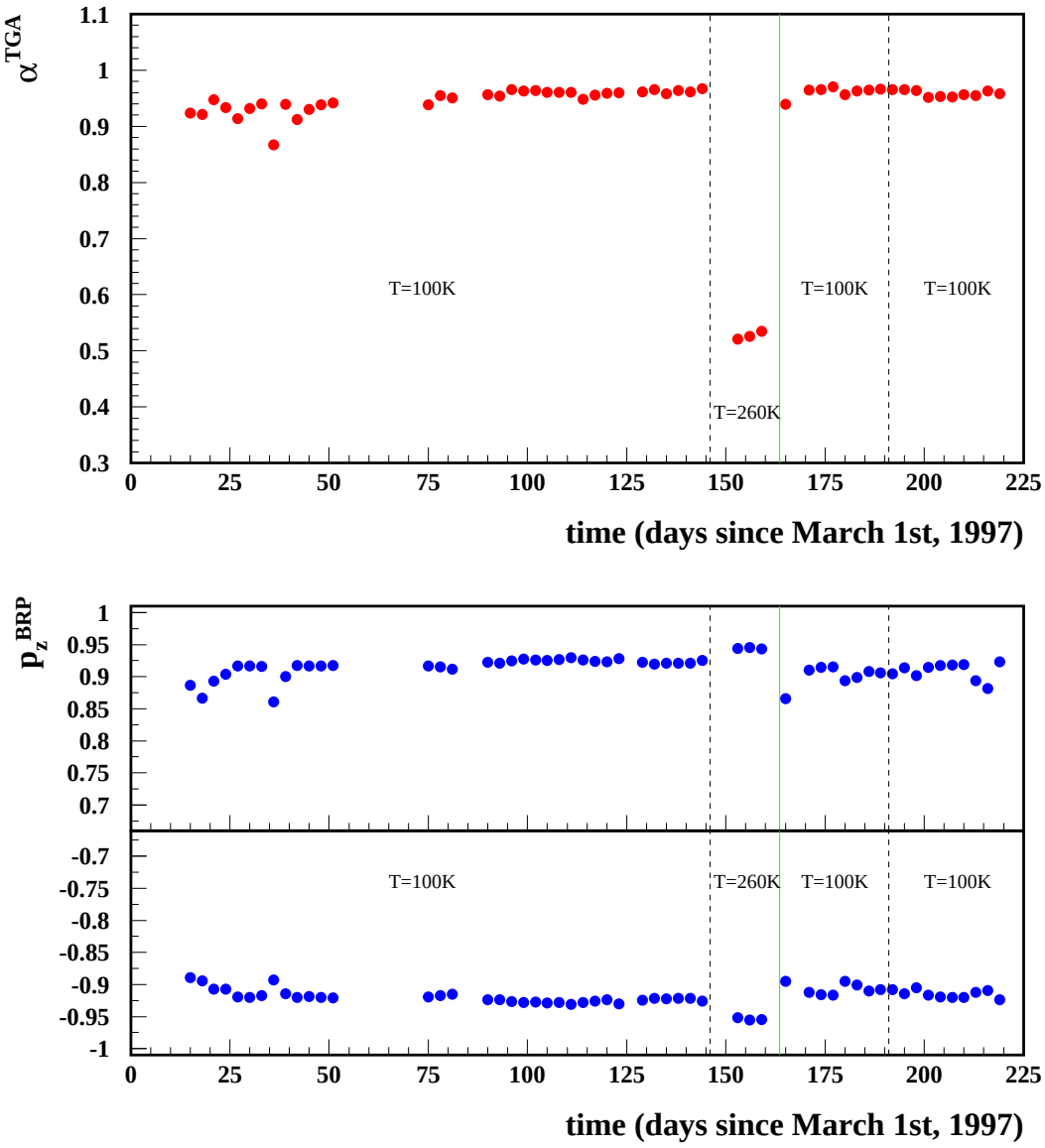

Fig. 14. The TGA (above) and BRP (below) measurements for the entire 1997 data taking period. The vertical dashed lines indicate HERA beam loss events which affected the cell surface properties, and the solid line indicates the replacement of the target cell.

In the period between January and June, the target was operated with only positive and negative states of nuclear vector polarization. From July on, a new injection mode combining vector and tensor polarization P_{z+}, P_{z-}, P_{zz+} and P_{zz-} was established in order to perform the first measurement of the tensor-polarized structure function b_1^d.

The average values for the four polarization states used in 2000 are the following:

$$P_{z+}^{T} = +0.851 \pm 0.029 \tag{56}$$
$$P_{z-}^{T} = -0.840 \pm 0.026 \tag{57}$$
$$P_{zz+}^{T} = +0.891 \pm 0.027 \tag{58}$$
$$P_{zz-}^{T} = -1.656 \pm 0.049 \tag{59}$$

Note that only the systematic uncertainty is quoted as the statistical uncertainty is negligible in comparison. The differences between the systematic uncertainties originate from the injection mode dependent systematic error of the atomic polarization.

The measured target density for this period, measured by means of the the spin-exchange collision relaxation method, is 2.1×10^{14} nucleons/cm^2.

6.2.1 Spin relaxation

The spin-flip probability per wall collision γ_z is proportional to τ_s^2, τ_s being the mean residence time: $\tau_s = \tau_0\, e^{\left(\frac{E_b}{kT}\right)}$ (see Eq. 27). Therefore γ_z should depend on the wall temperature T. In other words: if P_a^{BRP} does not change with T, this indicates vanishing wall depolarization within the experimental errors. In Fig. 16, a scan of the cell temperature down to very low temperatures is shown. The result indicates that no wall depolarization occurs. As a consequence, for the deuterium target the sampling correction for nuclear depolarization equals unity ($c_P = 1$), so that:

$$P_a = P_a^{BRP}. \tag{60}$$

Moreover, the calculated depolarization due to spin exchange collision resulted in a value $\Delta P_a^{se} = 0.3\,\%$. As in 2000 spin relaxation can be neglected completely, the polarization injected by the ABS equals the measured BRP value:

$$P_a^{inj} \simeq P_a^{BRP}. \tag{61}$$

6.2.2 Recombination

Although the atomic recombination is a strongly temperature dependent process, no variation of the measured atomic fraction α^{TGA} in a very wide rage around the working point $T_{cell} = 60\,\mathrm{K}$ was ever observed during the whole year. Fig. 17 (upper plot) reports a cell temperature scan performed in August. (For comparison a temperature scan performed with hydrogen in 1997 is also shown in the lower plot of the same figure). Additionally the measurement of the fraction of atoms surviving recombination, α_r^{TGA}, yielded the following

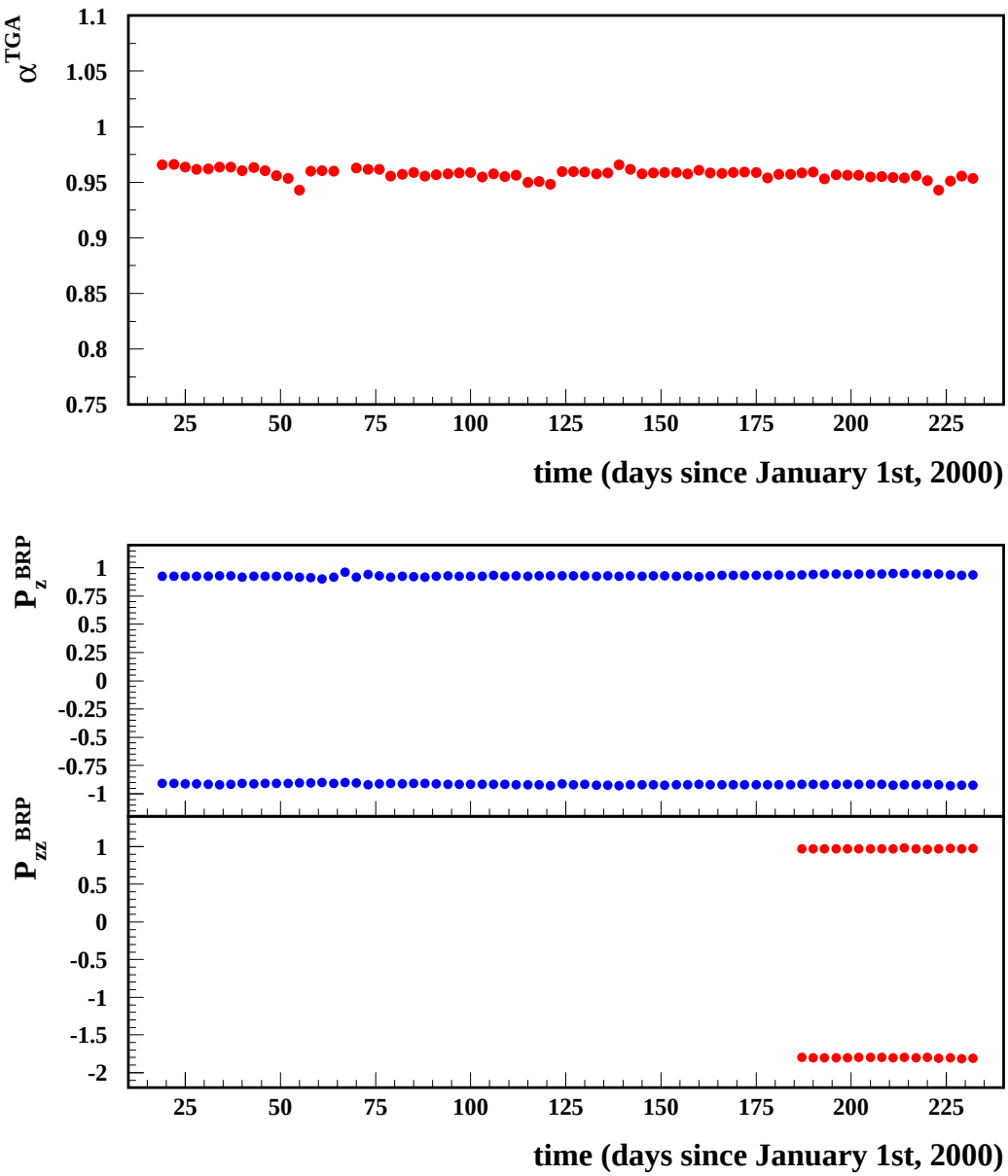

Fig. 15. Atomic fraction, α^{TGA} upper plot, and vector/tensor polarization, P^{BRP} lower plots, measured by TGA and BRP respectively during the year 2000 running period. Each symbol represents data averaged over a 72 hours bin. The absolute bin averaged values are always above 0.9. The tensor polarization (lower plot) was employed from July on.

average value:

$$\alpha_r^{TGA} = 0.997 \pm 0.014, \tag{62}$$

confirming that withing the measured uncertainty no evidence was found for contributions from recombined molecules. Therefore, for the deuturium data

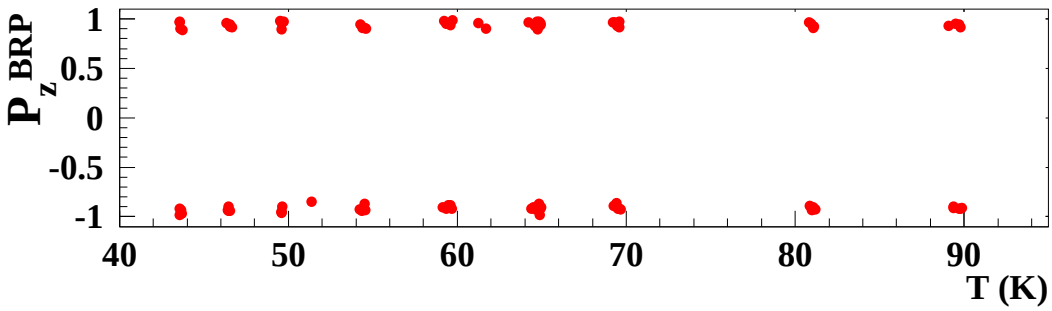

Fig. 16. Nuclear vector polarization P_z^{BRP} as function of the cell temperature T measured in August 2000. No dependence on the temperature can be observed. The operating temperature of the target during year 2000 data collection was 60 K.

taking period in 2000 both the sampling correction c_α and the impact of the uncertainty on β are negligible.

6.3 Transverse hydrogen running in 2002

During the 2002-2003 data taking period the HERMES transversely polarized hydrogen target worked in a very stable way. On the other hand, the poor performance of the HERA beam did not allow a detailed study of the bunch induced depolarization. Nevertheless, by scanning the target magnetic field a working point could be found where the loss of polarization due to the field non-uniformity was limited to 1.5 % at highest beam currents (25 mA). The average target polarization, $(P_{z+}^T - P_{z-}^T)/2$, during the 2002 data taking period was $P^T = 0.783 \pm 0.041$. This value is lower than that reported for the longitudinal hydrogen target (Section 6.1) mainly due to the lower applied target field.

The stability of the transverse target operation during 2002 running period is illustrated in Fig. 18. The target density in 2002 running period measured via spin-exchange collision was: 1.1×10^{14} nucl./cm^2.

7 Discussion

Table 8 summarizes averaged values for various target properties during the running periods.

A comparison between the longitudinally polarized hydrogen and deuterium target leads to the following conclusions. At the same guide field, in case of deuterium the spin exchange and wall relaxation processes are suppressed by

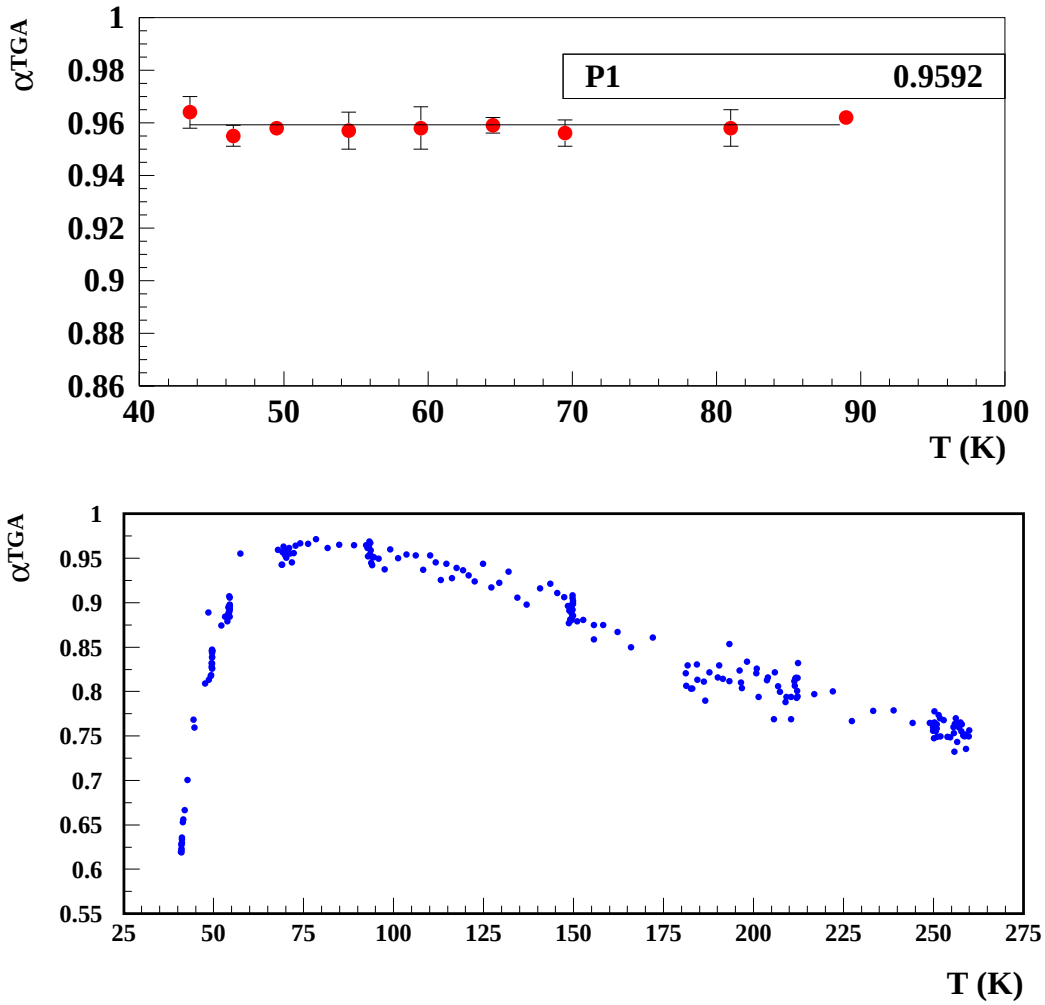

Fig. 17. Upper plot: measured atomic fraction as a function of the cell temperature for $T_{cell} < 100\,\mathrm{K}$ for the deuterium running in 2000. No dependence on the temperature can be seen. The working point during data taking was set to $T_{cell} = 60\,\mathrm{K}$. For comparison a temperature scan with hydrogen taken in 1997 is shown in the lower plot.

a factor $(B_C^H/B_C^D)^2 \simeq 20$ compared to hydrogen. The positive and negative P_z values for hydrogen coincide very well, while for deuterium there is a clear difference. This is due to the higher number of efficiencies and transmissions involved.

From the table it is possible to deduce the departures from the optimal performance like the amount of recombination ($\Delta\alpha_r = 1 - \alpha_r$), and the depolarization due to the different depolarizing mechansims: spin-exchange collisions (ΔP_{SE}), wall-depolarization (ΔP_{WD}) and beam-induced fields (ΔP_{BI}). The target density integrated over the cell length or areal density "t" is also shown together with a relative factor of merit (FOM) which takes into account both the polarization and the density. It is worthwhile to mention again that in

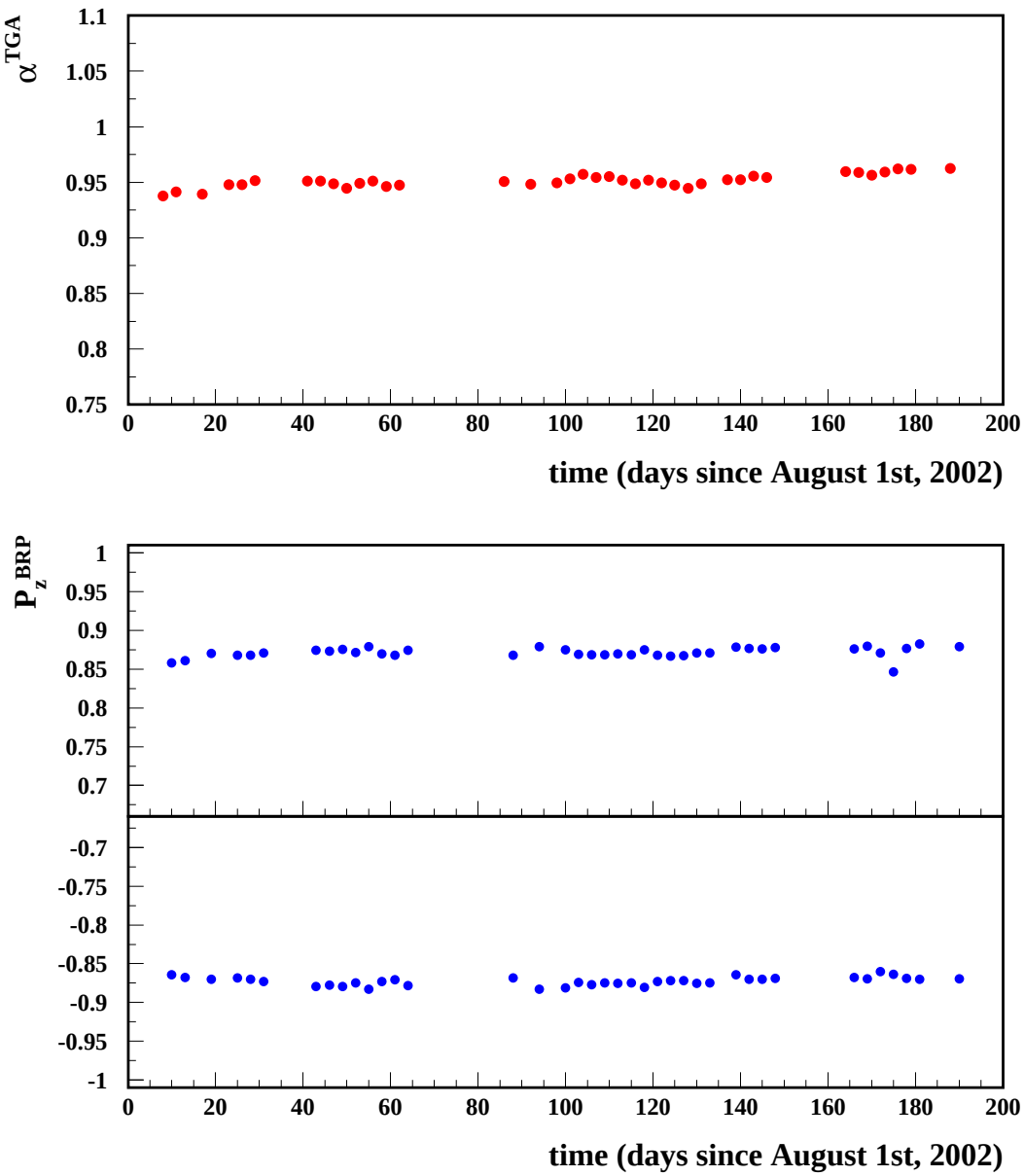

Fig. 18. The TGA (above) and BRP (below) measurements for the 2002/03 data taking period.

1997 the target cell had a larger cross-section ($29mm \times 9.8mm$) implying a higher conductance and a correspondingly lower density (about 40 %). The table illustrates once more the optimal performance of the $D_{||}$ target in 2000. For this target no recombination ($\Delta\alpha_r = 0$) and no depolarization phenomena ($\Delta P_{WD} = \Delta P_{SE} = \Delta P_{BI} = 0$) have been detected. This excellent behavior has to be attributed to the lower critical field of deuterium (11.7 mT) compared to hydrogen (50.7 mT), and to an improvement in the knowledge and preparation of the cell surface coating. The improved surface coating is also responsible for the better performance of the 2002 $H_{\perp}$ target compared to the

	$H_{\|\|}(1997)$	$H_{\perp}(2002)$	$D_{\|\|}(2000)$
α_0	0.960 ± 0.010	0.918 ± 0.032	0.919 ± 0.026
α_r	0.945 ± 0.035	0.979 ± 0.023	0.997 ± 0.017
P_{z+}	$+0.908 \pm 0.016$	$+0.859 \pm 0.032$	$+0.927 \pm 0.017$
P_{z-}	-0.908 ± 0.016	-0.859 ± 0.032	-0.915 ± 0.010
$-\Delta P_{SE}$	0.035	0.055	≤ 0.001
$-\Delta P_{WD}$	0.02	0.055	≤ 0.01
$-\Delta P_{BI}$	absent	0.015	absent
P_+^T	$+0.851 \pm 0.031$	$+0.783 \pm 0.041$	$+0.851 \pm 0.029$
P_-^T	-0.851 ± 0.031	-0.783 ± 0.041	-0.840 ± 0.026
t ($10^{14} nucleons/cm^2$)	0.7	1.1	2.1
FOM (P^2t) ($10^{14}/cm^2$)	0.5	0.67	1.5

Table 8
Summary of the HERMES target performance in the years 1997, 2000 and 2002. The tabulated values are averaged over the respective running periods. The ΔP_is are all polarization losses arising from the listed process. See text.

1997 $H_{||}$ target, as far as the amount of recombination is concerned.

On the other hand, in 2002, due the higher density obtained and the higher number of wall collisions, made spin-relaxation effects more important causing a loss in the polarization of about 11 %, thus limiting the gain in the factor of merit with respect to the 1997 running due to the increase in density. This indicates how an enhancement in the figure of merit of the target might be obtained by increasing the holding field proportionally with the density, in order to limit the spin relaxation effects.

8 HERMES results

In this last Section before the conclusions we would like to mention some of the measurements which have been possible with the polarized internal gaseous target during the different running periods.

The number of deep inelastic scattering events (after data quality cuts) collected with the different polarized targets are given in Tab. 9.

Between the different measurement which have been performed by the HERMES detector, we quote the following: the measurement of the g_1^p structure

target (year)	$DIS/milion$
$H_{\|\|}(1996-97)$	2.4
$D_{\|\|}(1998-2000)$	9.1
$H_{\perp}(2002-03)$	0.7

Table 9
Deep inelastic scattering events collected with the different polarized targets. The number are given in millions.

function [39]; the measurement of the g_1^d structure function [40]; the first measurement of the b_1^d structure function [41]; measurements of the quark-flavour decomposition [42,43]; the first measurement of single-spin asymmetries in deep-inelastic scattering off a transversely polarized target [44].

9 Conclusion

The HERMES polarized hydrogen and deuterium target has been reliably operating since 1996 providing high polarization and total systematic errors between 3 % and 4%. The systematics of both the recombination and depolarization processes in the storage cell are totally under control.

10 Acknowledgements

We gratefully acknowledge the DESY management for its support and the DESY staff and the staff of the collaborating institutions. This work was supported by the FWO-Flanders, Belgium; the INTAS contribution from the European Commission; the European Commission IHP program under contract HPRN-CT-2000-00130; the German Bundesministerium für Bildung und Forschung (BMBF); the Italian Istituto Nazionale di Fisica Nucleare (INFN); Monbusho International Scientific Research Program, JSPS, and Toray Science Foundation of Japan; the Dutch Foundation for Fundamenteel Onderzoek der Materie (FOM); the U.K. Particle Physics and Astronomy Research Council and Engineering and Physical Sciences Research Council; and the U.S. Department of Energy and National Science Foundation.

References

[1] HERMES Technical Design Report, DESY-PRC 93/06, 1993.

[2] K. Rith; *Progr. Part. Nucl. Phys* **49**, (2002), 245.

[3] A. A. Sokolov and I. M. Ternov, *Sov. Phys*, Doklady 8 (1964), 1203.

[4] D. P. Barber et al., Phys. Lett. B 343 (1995), 436.

[5] K. Ackerstaff et al.; *Nucl. Instr. Meth. A* **417**, (1998) 230.

[6] E. Steffens and W. Haeberli *Rep. Prog. Phys.* **66**, (2003) 1887.

[7] D. De Schepper et al.; *Nucl. Instrum Meth. A* **419**, (1998) 16.

[8] A. Nass, et al.; *Nucl. Inst. and Meth. A* **505**, (2003) 633.

[9] C. Baumgarten, et al.; *Nucl. Inst. and Meth. A* **496**, (2003) 277.

[10] C. Baumgarten, et al., *Nucl. Inst. and Meth A* **508**, (2003) 268.

[11] C. Baumgarten et al.; *Nucl. Inst. and Meth. A* **482**, (2002) 606.

[12] C. Baumgarten, et al.; *Nucl. Inst. and Meth A* **496**, (2003) 263.

[13] K. Ackerstaff, et al.; *Phys. Rev. Lett.* **82**, (1999) 1164.

[14] A. Airapetian et al., *Eur. Phys. J. D.* **29**, (2004) 21.

[15] C. Baumgarten et al.; *Eur. Phys. J. D* **18**, (2002) 37.

[16] C. Baumgarten, Ph. D. Thesis, University of Munich, Germany, DESY-THESIS-2000-038 (2000).

[17] G. E. Thomas et al.; *Nucl.Instrum. and Meth. A* **257**, (1987) 32.

[18] M. A. Bouchiat; *J. Phys. Radium***24**, (1963) 379.

[19] M. A. Bouchiat; *J. Phys. Radium***24**, (1963) 611.

[20] M. A. Bouchiat and J. Brossel; *Phys. Rev.***147**, (1965) 41.

[21] P. W. Anderson in *Magnetism vol. I*; G. T. Radio and H. Suhl (Edts.); Academic Press N. Y. (1963).

[22] N. Koch and E. Steffens *Rev. Sci. Instrum.* **70**, (1999) 1631.

[23] K. Halbach *Nucl.Instrum. and Meth. A* **169**, (1980) 213.

[24] D.Reggiani, Ph. D. thesis, University of Ferrara, Italy, DESY-THESIS-2003-001 (2003).

[25] S. Holloway; *Surf. Sci.***299/300**, (1994) 656.

[26] T. Engel and G. Ertl; *J. Chem. Phys.***69**, (1978) 1267.

[27] H. Conrad, G. Ertl and J. Küppers; *Surf. Sci.* **76**, (1978) 323.

[28] E. W. Kuipers et al.; *Phys. Rev. Lett.***66**, (1991) 116.

[29] C. T. Rettner; *Phys. Rev. Lett.***69**, (1992) 383.

[30] B. Braun Ph. D thesis MPIH - V25, Ludwig Maximilians-University, Munich, Germany (1995).

[31] J. S. Price and W. Haeberli; *Nucl. Instr. Meth. A***326**, (1993) 416.

[32] J. S. Price and W. Haeberli; *Nucl. Instr. Meth. A***349**, (1994) 321.

[33] H. Kolster Ph. D. thesis, Ludwig Maximilians-University, Munich, Germany (1998).

[34] E. M. Purcell and G.B. Fields; *Astrophys. J.***124**, (1956) 542.

[35] M. Desainfuscien and C. Auodoin; *Phys. Rev. A***13**, (1976) 2070.

[36] A. C. Allison *Phys. Rev. A***5**, (1972) 2695.

[37] J. F. J. van den Brand et al.; *Phys. Rev. Lett.* **78**, (1997) 1235.

[38] T. Wise et al.; *Phys. Rev. Lett.* **87**, (2001) 042701.

[39] A. Airapetian et al.; *Phys. Lett. B* **442**, (1998) 484.

[40] C. Weiskopf, Proceedings of the IX International Conference on Deep Inelastic Scattering and QCD (DIS 2001), Bologna - Italy, 2001.

[41] M. Contalbrigo, Proceedings of XV International Spin Physics Symposium (SPIN 2002), Brookhaven National Laboratory - NY (USA), 2002

[42] K. Ackerstaff et al., *Phys. Lett. B* **464**, (1999) 123.

[43] A. Airapetian et al., *Phys. Rev. Lett.* **92**, (2004) 012005.

[44] R. Seidl, Proceedings of the XII International Conference on Deep Inelastic Scattering and QCD (DIS 2004), Strbske Pleso - Slovakia, 2004.